An inter-organelle contact between endosomal GLP-1R, ER VAP-B, and the mitochondrial AKAP SPHKAP triggers PKA-dependent MIC19 phosphorylation and β-cell mitochondrial remodelling.

Gregory Austin[1,*], Liliane ElEid[1,*], Affiong I. Oqua[1,*], Yusman Manchanda[1], Yelyzaveta Poliakova[2], Karim Bouzakri[3], Alex Montoya[4], Dominic J. Withers[4,5], Ben Jones[6], Steven J. Millership[1], Inga Prokopenko[7,8] and Alejandra Tomas[1,#]

[1] Section of Cell Biology and Functional Genomics, Division of Diabetes, Endocrinology, and Metabolism, Department of Metabolism, Digestion and Reproduction, Imperial College London, London, United Kingdom.
[2] School of Public Health, Imperial College London, London, United Kingdom.
[3] Centre Européen d'Étude du Diabète, Strasbourg, France.
[4] MRC Laboratory of Medical Sciences, London, United Kingdom.
[5] Institute of Clinical Sciences, Faculty of Medicine, Imperial College London, London, United Kingdom.
[6] Section of Endocrinology and Investigative Medicine, Division of Diabetes, Endocrinology, and Metabolism, Department of Metabolism, Digestion and Reproduction, Imperial College London, London, United Kingdom.
[7] Department of Clinical and Experimental Medicine, University of Surrey, Guildford, United Kingdom.
[8] People-Centred Artificial Intelligence Institute, University of Surrey, Guildford, United Kingdom.

*Joint first authors

[#]Corresponding author: a.tomas-catala@imperial.ac.uk

Abstract

Glucagon-like peptide-1 receptor (GLP-1R) agonists (GLP-1RAs) ameliorate mitochondrial health by increasing its turnover and improving its quality control. While the GLP-1R is well known to stimulate cAMP production leading to activation of Protein Kinase A (PKA) and Exchange Protein Activated by cyclic AMP 2 (Epac2) signalling, there is a lack of understanding of the molecular mechanisms linking GLP-1RA-induced signalling with mitochondrial remodelling and improved mitochondrial function. Here we present a dataset that demonstrates that, following GLP-1RA stimulation in pancreatic β-cells, the GLP-1R interacts with endoplasmic reticulum (ER) membrane contact site (MCS) organising factor VAP-B from an endocytic location to engage SPHKAP, an A-kinase anchoring protein (AKAP) associated with type 2 diabetes (T2D) and adiposity in genome-wide association studies (GWAS), to trigger a pool of mitochondrially localised PKA signalling that phosphorylates the mitochondrial contact site and cristae organizing system (MICOS) complex component MIC19, enabling GLP-1RA-induced mitochondrial remodelling and optimal β-cell function.

Introduction

Maintenance of mitochondrial function is vital for the preservation of pancreatic β-cell regulated secretion of insulin[1], the main hormone in charge of lowering blood glucose concentrations, with disruptions in this process underlying the development and/or progression of type 2 diabetes (T2D)[2, 3] – an uncontrolled pandemic affecting ~500 million people worldwide, and causing ~1.5 million deaths per year[4]. The incretin glucagon-like peptide-1 (GLP-1), released from the gut during food intake, amplifies glucose-stimulated insulin release by binding to and activating its cognate G protein-coupled receptor (GPCR), the GLP-1 receptor (GLP-1R), triggering cAMP generation and downstream Protein Kinase A (PKA) and Exchange Protein Activated by cyclic AMP 2 (Epac2) signalling[5], a process that has been exploited to develop pharmacological GLP-1R agonists (GLP-1RAs) as T2D therapies. There is extensive data highlighting the beneficial role that GLP-1RAs have in the maintenance and/or restoration of mitochondrial function in β-cells and beyond, with reports emphasising their capacity to induce mitochondrial remodelling and turnover[6-9], a carefully orchestrated process essential for the preservation of optimal metabolic activity[10]. While a wide range of GLP-1R-induced pathways have been reported, there is no clear description of a unifying mechanism that explains how the GLP-1R modulates mitochondrial remodelling and function. Here, we present new evidence in β-cells and primary islets demonstrating that, following agonist binding and internalisation, endosomal GLP-1R binds to endoplasmic reticulum (ER)-localised ER-mitochondria membrane contact site (ERMCS) organising factor VAP-B to engage the mitochondrial A-kinase anchoring protein (AKAP) SPHKAP, whose gene coding variants are linked to type 2 diabetes (T2D) and high BMI in genome-wide association studies (GWAS). Establishment of a tripartite membrane contact site (MCS) between GLP-1R-positive endosomes, ER VAP-B and mitochondrial SPHKAP leads to the generation of a pool of mitochondrially localised PKA activity that triggers PKA-dependent phosphorylation of the mitochondrial contact site and cristae organizing system (MICOS) complex component MIC19, enabling GLP-1RA-induced mitochondrial remodelling and functional preservation, and significantly contributing to the potentiation of β-cell insulin secretion and survival under ER stress by the GLP-1R. This is, to our knowledge, the first description of a three-way contact between an endosomal GPCR, the ER-resident MCS organiser VAP-B and a mitochondrial AKAP, enabling the generation of a highly localised PKA signalling hub to control the function of the MICOS complex, and therefore cristae architecture and mitochondrial turnover, with potential effects in the regulation of mitochondrial lipid metabolism. Our data not only unveils a previously unknown pathway that channels Gαs-coupled GPCR signalling into mitochondria, but also uncovers the molecular mechanism employed by GLP-1RAs to achieve mitochondrial regeneration and optimised β-cell function, with important repercussions for disorders such as T2D, obesity, and neurodegeneration, where the GLP-1R plays prominent roles.

Results

β-cell GLP-1R interactome reveals functionally relevant binding of active GLP-1R with VAP-B.

To gain a comprehensive understanding of the specific partners engaged by active GLP-1R in β-cells, we performed an interactome analysis of proteins binding to the receptor in vehicle *versus* 5-minute exendin-4-stimulated conditions in the rat INS-1 832/3 β-cell line (Fig. 1). Mass spectrometry (MS) analysis of receptor co-immunoprecipitants revealed a list of proteins enriched in stimulated *versus* unstimulated conditions (Fig. 1a,b, Extended Data Fig. 1a). Gene ontology analysis of the identified factors indicated that these were enriched in pathways related to endomembranes and the endoplasmic reticulum (ER) (Extended Data Fig. 1b). Amongst the identified factors, we found a high number of proteins known to be

localised to ER-mitochondrial membrane contact sites (MCSs) (Fig. 1c), which are points of close interaction, but not fusion, between distinct organelle membranes that fulfil specific functions, including cross-organelle ion and/or lipid sensing and transfer, and signal transmission to coordinate organelle biogenesis[11]. While known active GLP-1R interactors such as $G_{\alpha S}$, AP2, Rab5, and β-arrestin 2 were, as expected, identified in our interactomic list, the most prominently enriched interactor for active *versus* inactive GLP-1R was VAMP Associated Protein B (VAP-B), followed by its homolog VAP-A, integral ER proteins whose main role is the establishment and maintenance of organelle-ER interactions or membrane contact sites (MCSs)[12, 13], including with endosomes and mitochondria. We next validated the GLP-1R – VAP-B binding MS results by co-immunoprecipitation of both EGFP-VAP-B (Fig. 2a,b) and endogenous VAP-B (Fig. 2c,d) with SNAP and FLAG-tagged human GLP-1R in vehicle *versus* 5-minute exendin-4-stimulated INS-1 832/3 cells. Confocal microscopy analysis of exendin-4-stimulated GLP-1R and EGFP-VAP-B co-localisation in these cells revealed that GLP-1R-positive endosomes were intimately associated with VAP-B-positive ER network regions, with the ER network often surrounding a central core of GLP-1R-positive signal (Fig. 2e), indicating that GLP-1R-positive endosomes establish close contacts with VAP-B-positive ER membranes, and suggesting a potential localisation of the receptor to endosome-ER MCSs, a possibility that we validated by transmission electron microscopy (TEM) localisation of exendin-4-stimulated gold-labelled GLP-1R to these contact sites (Extended Data Fig. 2a). The interaction of active GLP-1R with VAP-B was functionally relevant, as it was no longer present when VAP-B P56S, a self-aggregating loss-of-function VAP-B mutant associated with amyotrophic lateral sclerosis (ALS)[14, 15] was expressed instead of its wildtype counterpart (Fig. 2f,g), and both VAP-B knockdown by RNAi (Fig. 2h, Extended Data Fig. 2b,c), and expression of VAP-B P56S, but not of wildtype VAP-B (Fig. 2i), significantly reduced the capacity of the GLP-1R to potentiate insulin secretion from INS-1 832/3 cells.

Active GLP-1R – VAP-B binding requires receptor internalisation and is differentially modulated by GLP-1RAs with varying GLP-1R internalisation propensities.

To elucidate whether active GLP-1R binding to VAP-B requires its prior internalisation, we co-transfected INS-1 832/3 cells stably expressing SNAP/FLAG-tagged human GLP-1R with dominant negative (K44A) mutants of dynamin 1 and 2 to block receptor endocytosis following its stimulation with exendin-4 (Fig. 3a). Under these conditions, increased binding of the receptor to VAP-B in stimulated *versus* vehicle conditions was abrogated (Fig. 3b), demonstrating that the GLP-1R interacts with VAP-B only following its agonist-induced internalisation. Supporting this notion, MS interactomic analyses of GLP-1R co-immunoprecipitates in INS-1 832/3 cells following 5-minute stimulation with endogenous agonist GLP-1, as well as with the exendin-4-based biased GLP-1RAs exendin-F1 and exendin-D3, previously shown to trigger opposed degrees of GLP-1R internalisation[16, 17], resulted in marked differences in the propensity for the receptor to associate with VAP-B (Extended Data, Fig. 3), with agonists that trigger robust receptor internalisation (GLP-1, exendin-4, exendin-D3) showing a much stronger degree of GLP-1R - VAP-B interaction compared to low GLP-1R-internalising exendin-F1. Marked kinetic differences in GLP-1R – VAP-B binding following exendin-4 *versus* exendin-F1 stimulation were also demonstrated in INS-1 832/3 cells by a novel nanoBRET assay with nanoluciferase-tagged GLP-1R co-expressed with Venus-tagged VAP-B (Fig. 3c,d). We extended our analysis to a panel of seven different GLP-1RAs, including, as well as exendin-4, exendin-F1 and exendin-D3, fatty acid-modified semaglutide[18] and tirzepatide[19], as well as small molecules orforglipron[20] and danuglipron[21]. We first tested these GLP-1RAs for their capacity to induce GLP-1R internalisation in purified mouse islets transduced with SNAP/FLAG-tagged human GLP-1R adenoviruses (Fig. 3e). As previously shown, acute (5-minute) exposure to exendin-4 and exendin-D3 triggered noticeable GLP-1R internalisation, while this was not evident for this stimulation time with biased agonist exendin-F1. Additionally, and as previously published[22], semaglutide displayed a much more robust GLP-1R internalisation than tirzepatide, an

agonist that shows a similar degree of GLP-1R $G_{\alpha S}$ bias as exendin-F1. We also detected a clear difference in GLP-1R internalisation triggered by orforglipron *versus* danuglipron, with the latter showing a similar level of receptor internalisation to that triggered by exendin-4, while the former did not trigger any detectable internalisation after 5 minutes of agonist exposure. Levels of VAP-B co-immunoprecipitation using the GLP-1RAs described above demonstrated that GLP-1R – VAP-B binding closely correlates with the level of receptor internalisation triggered by each of the evaluated GLP-1RAs (Fig. 3f,g).

Active GLP-1R associates with ER-mitochondria MCSs and triggers mitochondrially localised PKA activity.

As stated above, besides VAP-B, our interactome analysis highlighted several factors enriched for their association with active *versus* inactive GLP-1R located at ER-mitochondrial MCSs (ERMCSs) (Fig. 1c), a location where VAP-B plays a prominent organising role[15], suggesting that this could be a potential hub for endosomal GLP-1R signalling. To visualise a possible association of GLP-1R with ERMCSs, we employed a split-GFP-based contact site sensor (SPLICS)[23] to specifically detect these contacts in conjunction with exendin-4-stimulated GLP-1R in INS-1 832/3 cells (Fig. 4a). This approach allowed us to observe an intimate association between GLP-1R-positive endosomes and ERMCSs in these cells, validating our previous hypothesis. Next, and given that the main signalling output from the receptor is the downstream activation of PKA, and the known importance of mitochondrial PKA signalling in the control of mitochondrial function[24], we evaluated whether signalling from the GLP-1R would trigger a pool of mitochondrially localised PKA activity using either whole cell (Fig. 4 b,c) or mitochondrially restricted (Fig. 4d,e) subcellular PKA biosensors[25]. Exendin-4 stimulation of INS-1 832/3 cells triggered, as expected, a robust global PKA response, which was also evident with the mitochondrially-localised PKA biosensor, demonstrating that GLP-1R stimulation triggers mitochondrial PKA activity.

Active GLP-1R engages the mitochondrial AKAP SPHKAP via binding to VAP-B.

Amongst the interactors enriched for active GLP-1R in our MS interactome analysis, we identified the A-kinase anchoring protein (AKAP) SPHKAP (Fig. 4f), a paralog of AKAP11 that binds two RI subunits of the PKA holoenzyme[26], with both SPHKAP and AKAP11 previously shown to localise to mitochondria (SPHKAP)[27], or to regulate mitochondrial metabolism (AKAP11)[28]. Both SPHKAP and AKAP11 also harbour a FFAT (two phenylalanines in an acidic tract) motif[29, 30], a specific protein sequence that binds to the Major Sperm Protein (MSP) domain of VAPs[31]. We first demonstrated that SPHKAP localises to mitochondria in β-cells by confocal microscopy co-localisation of wildtype SPHKAP-EGFP with the mitochondrial marker Mitotracker Red in INS-1 832/3 cells (Fig. 4g, top panels). Next, we generated a mutant version of SPHKAP-EGFP harbouring a point mutation in its FFAT motif (A215E, DFLT**A**SE to DFLT**E**SE) to disrupt any potential binding of SPHKAP to VAP-B. SPHKAP-EGFP FFAT motif mutant displayed a complete loss of mitochondrial localisation, with fluorescence signal now dispersed homogeneously across the cytoplasm (Fig. 4g, bottom panels), demonstrating that SPHKAP localisation to mitochondria depends on its binding to VAP-B via its FFAT motif.

SPHKAP is expressed in metabolically relevant tissues, including pancreatic islets and intestinal K- and L-cells, and contributes to both incretin secretion and incretin-dependent glucoregulation[32, 33]. We found decreased levels of SPKHAP mRNA in a published RNA Seq database of islets from *db*/*db* *versus* wildtype mice (Extended Data, Fig. 4a) and genome-wide significant associations between *SPHKAP* gene variants, risk of type 2 diabetes (T2D) and higher BMI in meta-analyses from four separate genome-wide association studies (GWAS) in humans[34-37] (Extended Data, Fig. 4b-e). The extent of the effect of associated *SPHKAP* variants in T2D *versus* BMI was tightly correlated (Fig. 5a), suggesting a shared

pathway for SPHKAP in both disorders. Additionally, our own genetic analysis demonstrated a significant association between *SPHKAP* gene coding variants and random blood glucose levels in UK Biobank (UKBB) individuals without diabetes from whole exome sequencing (WES) data (Fig. 5b), strongly supporting a role for SPHKAP in the regulation of β-cell function.

To investigate the potential involvement of SPHKAP in GLP-1R-induced mitochondrial PKA signalling, we first validated our previously identified GLP-1R – SPHKAP interaction by co-immunoprecipitation of endogenous SPHKAP (Fig. 5c) and SPHKAP-EGFP (Fig. 5d, control RNAi lanes) with GLP-1R in vehicle *versus* exendin-4-stimulated INS-1 832/3 cells. We also determined that this interaction requires VAP-B, as it is abrogated following VAP-B knockdown (Fig. 5d, VAP-B RNAi lanes). Finally, we also observed the loss of SPHKAP-EGFP binding to exendin-4-stimulated GLP-1R for the FFAT-mutant SPHKAP DFLT**E**SE (Fig. 5e), demonstrating that SPHKAP interaction with VAP-B is required for this AKAP to engage with active GLP-1R at ERMCSs.

Mitochondrially-localised GLP-1R signalling requires SPHKAP and controls PKA-dependent MIC19 phosphorylation, mitochondrial function, and morphology.

We next tested the effect of SPHKAP knockdown on GLP-1R control of mitochondrial function. SPHKAP knockdown efficiency in INS-1 832/3 cells was validated against both endogenous SPHKAP (Extended Data, Fig. 5a) and SPHKAP-EGFP (Extended Data, Fig. 5b). Loss of SPHKAP did not affect the interaction between the receptor and VAP-B (Extended Data, Fig. 5c,d), indicating that the GLP-1R is recruited to VAP-B-positive ERMCSs by other means independent of SPHKAP. Loss of SPHKAP did not affect the capacity for the receptor to generate cAMP following exendin-4 stimulation (Extended Data, Fig. 5e). In contrast, while global PKA responses where not significantly affected by SPHKAP knockdown (Extended Data, Fig. 5f), exendin-4-induced mitochondrial PKA activity was blunted (Fig. 6a). Additionally, while we measured a small increase in mitochondrial membrane potential following exendin-4 stimulation in control conditions, this response, as well as subsequent membrane potential rises triggered by high glucose exposure, were reduced in SPHKAP RNAi-treated *versus* control cells (Fig. 6b). Moreover, ATP levels downstream of exendin-4 exposure were significantly reduced in absence of SPHKAP (Fig. 6c), suggesting a defect in GLP-1R-dependent control of mitochondrial function. As SPHKAP has previously been shown to bind to the mitochondrial cristae junction regulator and MICOS complex component MIC19[27], a prominent PKA substrate involved in cristae assembly during mitochondrial remodelling[38], as well as in ERMCSs formation[39], we next tested whether exendin-4 stimulation would trigger MIC19 phosphorylation in INS-1 832/3 cells, using an antibody raised specifically against PKA phospho-site RRxpS/T[40]. Results showed that 5 minutes of exendin-4 exposure resulted in a ~5-fold increase in PKA-specific MIC19 phosphorylation, an effect that was potentiated by the adenylate cyclase activator forskolin (Fig. 6d,e). Furthermore, knockdown of either SPHKAP or VAP-B in INS-1 832/3 cells led to the loss of exendin-4-induced MIC19 phosphorylation, demonstrating that the GLP-1R engages SPHKAP at VAP-B-positive ERMCSs to phosphorylate this MICOS complex component (Fig. 6f). As the main role of MIC19 is to orchestrate mitochondrial cristae assembly[41] during mitochondrial remodelling, we next assessed whether GLP-1R stimulation would play a role in mitochondrial remodelling in INS-1 832/3 cells, and whether this would be affected by SPHKAP knockdown. Mitochondrial morphology assessments showed that 5-minute exendin-4 exposure triggered acute mitochondrial remodelling in these cells, resulting in reduced mitochondrial mean form factor and area, and that both basal mitochondrial morphology and exendin-4-induced mitochondrial remodelling were disturbed by SPHKAP knockdown (Fig. 6g,h).

Loss of SPHKAP impairs GLP-1R-dependent potentiation of insulin secretion and β-cell survival under ER stress.

We next determined the impact of the previously identified phenotypes on β-cell function by analysing insulin secretion and β-cell survival to ER stress exposure downstream of GLP-1R stimulation in SPHKAP RNAi-treated *versus* control cells. Exendin-4-stimulated insulin secretion was indeed significantly reduced in SPHKAP RNAi *versus* control RNAi treated INS-1 832/3 cells (Fig. 7a), and the anti-apoptotic effect of exendin-4 in thapsigargin-exposed cells was blunted following SPHKAP knockdown (Fig. 7b).

Interaction between endogenous GLP-1R, VAP-B and SHPKAP in primary mouse and human islets.

Finally, we validated the previously identified interactions between GLP-1R, and either VAP-B or SPHKAP in primary tissue with endogenous receptor expression by proximity ligation assays performed in purified primary mouse and human islets (Fig. 8a,b, Extended Data Fig. 6), using one of the few existing validated mouse or human GLP-1R antibodies from the Developmental Studies Hybridoma Bank[42-44], with GLP-1R – VAP-B and GLP-1R – SPHKAP interactions readily observed in both exendin-4-stimulated mouse and human islets. We also replicated mitochondrial morphology assessments in dispersed (to increase siRNA uptake) islets from wildtype mice transfected with control *versus* SPHKAP RNAi (Fig. 8c,d). Results in these primary islet cells again showed an effect of acute (5-minute) exendin-4 exposure on mitochondrial remodelling, resulting, as in INS-1 832/3 cells, in reduced mitochondrial mean area and a tendency for reduced mitochondrial form factor downstream of GLP-1R activation, and with both basal mitochondrial morphology and GLP-1R-induced remodelling altered by SPHKAP knockdown.

Discussion

Mitochondrial malfunction is a prominent feature of diabetes, englobing defects in mitochondrial structure and dynamics, reactive oxygen species overproduction and apoptosis, breakdown of nutrient sensing, and metabolic uncoupling[45, 46], with strong backing evidence from human genetic studies[47-49]. Strategies to control the detrimental effect of T2D in affected tissues are likely to involve the amelioration of mitochondrial function, with GLP-1RAs being no exception, with numerous reports highlighting their capacity to potentiate mitochondrial quality control mechanisms and improve mitochondrial health[6-9]. Despite the accumulating evidence around pathways engaged by incretin receptors and other GPCRs to exert their effects in target tissues, there is still considerable uncertainty on the precise molecular mechanisms that they employ, particularly with regards to the spatiotemporal organisation of their signalling and their presence in spatially restricted subcellular signalling hubs or nanodomains[50]. In this context, the study of MCSs has become an area of considerable importance to understand the spatial architecture of subcellular signalling, with recent reports increasingly recognising their prominent role, including in pancreatic β-cells, where they underscore processes ranging from insulin granule biogenesis to calcium homeostasis[51-53]. Here, we took an unbiased approach to unveil new molecular partners that might work in concert with the GLP-1R to generate some of the known receptor responses in β-cells, finding not only that the receptor engages a MCS-based mechanism to organise its signalling, but that the main constituents of these inter-organelle contacts, namely the VAPs, are by a considerable margin the most prominent intracellular partners of active endosomal GLP-1R. This suggests that the engagement of active GLP-1R with the ER and the subsequent generation of ER-localised signalling is the main role for intracellular GLP-1Rs once the first wave of signalling from the plasma membrane has ensued, and suggests that GLP-1RAs with different receptor internalisation *versus* lysosomal degradation propensities might regulate the kinetics of this engagement, including the potential prolongation of this interaction over time by slow internalising compounds despite the initially reduced acute engagement seen in the present study.

We furthermore have unveiled the engagement of the receptor with ERMCSs, where we describe the formation of a novel tripartite inter-organelle contact and signalling hub constituted by endosomal GLP-1R, ER-resident VAP-B, and the mitochondrial AKAP SPHKAP, with VAP-B playing a central role as a tethering factor responsible for the separate recruitments of GLP-1R and SPHKAP, the latter via its direct interaction with SPHKAP FFAT motif, while the former is likely to involve currently unidentified intermediary factors as no typical FFAT motif is present in the primary sequence of GLP-1R. We also confirm SPHKAP itself as a mitochondrial AKAP in β-cells, where we reveal the important role that this PKA anchoring protein plays in the control of mitochondrial function downstream of GLP-1R activity, opening the door for other $G_{\alpha s}$-coupled GPCRs to also act via VAP-B and SPHKAP to control β-cell mitochondrial PKA activity and function.

The relevance of SPHKAP for the control of β-cell function is supported by human genetic data of genome-wide significance unveiling an association between *SPHKAP* gene variants and random blood glucose levels as well as T2D risk, while we additionally observe a correlation between the effect of these variants in T2D and BMI (as a proxy for obesity), indicating that SPHKAP plays a pleiotropic role in the development of both disorders, and suggesting the engagement of common SPHKAP-dependent signalling pathways, which could potentially involve the GLP-1R interacting with VAP-B and SPHKAP in both anorectic neurons and pancreatic β-cells, or alternatively involve other GPCRs acting via VAP-B and SPHKAP to modulate mitochondrial function in other tissues, for example in fat and liver where this mechanism might regulate energy expenditure, a possibility supported by the previously published interaction between the closely related glucagon receptor and VAP-B in hepatocytes[54]. In any case, the significance of the engagement of SPHKAP to VAP-B-positive ERMCSs is likely to surpass the β-cell, with expression of this AKAP, as well as its FFAT motif-containing ortholog AKAP11, in other tissues such as liver, brain and heart[26, 55], likely reflecting similar mechanisms of control of GPCR-induced ERMCS-localised PKA activity in those tissues. In this regard, it would be highly relevant to investigate whether the known effects of GLP-1RAs in neurodegenerative disorders such as Alzheimer's disease involve mitochondrial health improvement via the VAP-B – SPHKAP pathway in GLP-1R-expressing astrocytes, where the receptor has already been demonstrated to act as a regulator of mitochondrial dysfunction via the cAMP/PKA pathway[56].

We would also like to highlight our identification of the MICOS complex protein MIC19 as a target for VAP-B- and SPHKAP-dependent PKA phosphorylation downstream of GLP-1R activity, as this protein is not only a key member of the mitochondrial cristae junctions, and therefore responsible for the organisation of mitochondrial inner and outer membrane contacts and overall architecture of respiratory complexes as well as the mitochondrial proton pump, but it has also been recently unveiled to play a prominent role in the formation of ERMCSs, where it enables the transfer of lipid precursors for the biosynthesis of the key mitochondrial lipid cardiolipin[57], therefore connecting mitochondrial cristae organisation with the generation of cristae membrane curvature and the control of mitochondrial function afforded by cardiolipin[39]. We therefore hypothesise that GLP-1R-dependent phosphorylation of MIC19 via the VAP-B – SPHKAP – PKA pathway might not only indicate a direct role for the receptor in controlling cristae architecture and mitochondrial turnover, but also in the regulation of lipid precursor transfer across ERMCSs to meet the β-cell requirement for cardiolipin synthesis to sustain mitochondrial turnover and renewal at times of high metabolic demand, particularly as alterations in cardiolipin profiles have been reported in several diseases where GLP-1RAs play beneficial roles, such as Alzheimer's, Parkinson's, obesity, and T2D[58].

Beyond VAP-B and SPHKAP, our interactome reveals the association of active GLP-1Rs with other ER and/or mitochondrial factors. Amongst those, there is a noticeable enrichment

in lipid enzymes, including lipases and their regulators (Copb1, Mest), cholesterol synthesis, metabolism and transport factors (Dhcr7, Hmgcr, Pgrmc1, Por, Ptdss1), lipid biosynthesis enzymes and their regulators (TMEM120A, Acsl4, Fads1, Chp1, Cds2, Cdipt, AGPAT4, Tamm41, Bdh1), and mitochondrial fatty acid β-oxidation enzymes (HADHA/B), as well as the ER-lipid droplet MCS small GTPase Rab18[59], suggesting a more general involvement of ERMCS-localised GLP-1R signalling in the control of β-cell lipid handling, perhaps as a means to control lipid detoxification and energy expenditure under the toxic fuel-excess environment that underscores β-cell dysfunction during T2D[60]. Finally, beyond lipid enzymes, the GLP-1R also interacts with the ERMCS components Sarcoendoplasmic Reticulum Calcium ATPase (SERCA) pump[61] in the ER, and voltage-dependent anion-selective channel protein 2 (VDAC2) in the mitochondrial outer membrane, both involved in calcium transfer across ERMCSs[62], suggesting a prominent role for the receptor in the control of calcium homeostasis, with predicted important implications for the regulation of mitochondrial function and ER stress responses, as well as potentially linked to increased energy expenditure via futile calcium cycling mechanisms[63].

In summary, this investigation has unveiled the existence of a novel multi-organelle signalling platform in pancreatic β-cells involving active GLP-1R in endosomes, VAP-B in the ER, and SPHKAP in mitochondria, whose role is to enable localised PKA activity in mitochondria to phosphorylate the MICOS complex and ERMCS component MIC19, with important implications for the control of β-cell mitochondrial function and remodelling, and potentially regulating the transfer of lipids between the ER and mitochondria.

Online Methods

Cell culture

INS-1 832/3 rat insulinoma cells were maintained in RPM1-1640 at 11 mM D-glucose, supplemented with 10% fetal bovine serum (FBS), 10 mM HEPES, 2 mM L-glutamine, 1 mM pyruvate, 50 µM β-mercaptoethanol, and 1% penicillin/streptomycin. INS-1 832/3 cells stably expressing SNAP/FLAG-tagged human GLP-1R (hGLP-1R) were generated by transfection of pSNAP-GLP-1R (Cisbio) into INS-1 832/3 cells lacking endogenous GLP-1R expression (a gift from Dr Jacqueline Naylor, AstraZeneca[64]) followed by G418 (1 mg/ml) selection. Mycoplasma testing was performed yearly. Cell culture reagents were obtained from Sigma or Thermo Fisher Scientific.

Peptides and fluorescent probes

GLP-1 was purchased from Bachem, semaglutide from Imperial College London Healthcare NHS Trust pharmacy, and tirzepatide was a gift from Sun Pharmaceuticals. Custom analogues were from WuXi AppTec, China, and danuglipron and orforglipron were purchased from MedChemExpress. SNAP-Surface fluorescent probes were from New England Biolabs and MitoTracker™ Red CMXRos from Thermo Fisher Scientific.

GLP-1R interactome

INS-1 832/3 SNAP/FLAG-hGLP-1R cells were stimulated with vehicle or 100 nM GLP-1RA (GLP-1, exendin-4, exendin-F1 or exendin-D3) for 5 minutes. Following stimulation, a 6-cm dish of cells from each condition was washed with PBS and osmotically lysed in lysis buffer (50 mM Tris-HCl, pH 7.4, 150 mM NaCl, 1% Triton X-100, 1 mM EDTA) with 1% protease inhibitor (Roche) and 1% phosphatase inhibitor cocktail (Sigma-Aldrich) at 4°C. The cell lysates were centrifuged at 12,000 g and 4°C for 10 minutes, prior to the addition of 40 µl of anti-FLAG M2 beads (A2220, Sigma-Aldrich) for overnight rotating incubation at 4°C to increase binding efficiency. Samples were centrifuged at 5,000 g for 30 seconds, and bead

pellets washed three times in 500 µl wash buffer (50 mM Tris-HCl, 150 mM NaCl, pH 7.4), before storage at -80°C until further analysis.

Beads were resuspended in 150 µl 1 M urea in 20 mM HEPES pH 8.0, 1 mM DTT followed by addition of 1.5 µg of Trypsin gold (Promega) with overnight digestion at 37°C. Supernatants were subsequently acidified with 0.5% trifluoroacetic acid (TFA), followed by desalting using reversed-phase spin tips (Glygen Corp) and dried using vacuum centrifugation. Dried peptides were resuspended in 0.1% TFA and Liquid Chromatography Tandem Mass Spectrometry (LC-MS/MS) performed as previously described[65] using an Ultimate 3000 nano-HPLC coupled to a Q-Exactive mass spectrometer (Thermo Scientific) via an EASY-Spray source. Peptides were loaded onto a trap column (Acclaim PepMap 100 C18, 100 µm × 2 cm) at 8 µl/min in 2% acetonitrile, 0.1% TFA. Peptides were then eluted on-line to an analytical column (Acclaim Pepmap RSLC C18, 75 µm × 75 cm). A 90-minute stepped gradient separation was used with 4-25% acetonitrile 80%, formic acid 0.1% for 60 minutes, followed by 25-45% for 30 minutes. Eluted peptides were analysed by Q-Exactive operating in positive polarity and data-dependent acquisition mode. Ions for fragmentation were determined from an initial MS1 survey scan at 70,000 resolution (at m/z 200), followed by higher-energy collisional dissociation of the top 12 most abundant ions at a resolution of 17,500. MS1 and MS2 scan AGC targets were set to 3e6 and 5e4 for a maximum injection time of 50 msec and 75 msec, respectively. A survey scan m/z range of 350 – 1800 m/z was used, with a normalised collision energy set to 27%, minimum AGC of 1e3, charge state exclusion enabled for unassigned and +1 ions and a dynamic exclusion of 45 seconds.

Data was processed using the MaxQuant software platform (v1.6.10.43)[66], with database searches carried out by the in-built Andromeda search engine against the Swissprot Rattus Norvegicus database (Downloaded – 21st May 2022, entries: 8,132) concatenated with the human GLP1R protein sequence. A reverse decoy database approach was used at a 1% FDR for peptide spectrum matches and protein identifications. Search parameters included: maximum missed cleavages set to 2, variable modifications of methionine oxidation, protein N-terminal acetylation, asparagine deamidation and cyclisation of glutamine to pyroglutamate.

Label-free quantification was enabled with an LFQ minimum ratio count of 1. Proteins were filtered for those containing at least one unique peptide and identified in all 4 biological replicates. For normalisation, proteins were ranked by fold change increase in abundance compared with control (vehicle-treated) immunoprecipitates. The resulting data was pre-processed by elimination of proteins that are non-specifically bound and residual background proteins, such as common contaminants and reverse database proteins. To further facilitate the selection of GLP-1R interactors, the following criteria were established; i) identified at least twice from four runs; ii) not nuclear proteins; and (iii) previously identified in pancreatic β-cells.

Untargeted label-free quantitation (LFQ) intensity values, normalised to hGLP-1R levels in each immunoprecipitated sample, were analysed by LFQ Analyst[67] to identify differences in levels of individual protein-GLP-1R interactions between vehicle- and GLP-1RA-treated conditions. Paired t-tests adjusted for multiple comparisons using Benjamin-Hochberg false discovery rate correction and Perseus type imputations were used for statistical analysis. To generate novel information about the functional pathways represented by these potential GLP-1R interactors, we performed pathway enrichment analysis with GLP-1R binding partners exhibiting changes between vehicle and exendin-4-stimulated conditions using gProfiler.

cDNA and siRNA transfection

INS-1 832/3 cells were transfected with relevant amounts of plasmid cDNA outlined in Table 1 or siRNA outlined in Table 2 using Lipofectamine 2000 (Life Technologies) in media without antibiotics according to the manufacturer's instructions. Experiments were carried out 24-48 hours after plasmid cDNA and 72 hours after siRNA transfection.

Name	Origin	Assay
EGFP-VAP-B	Gift from Dr Emily Eden, UCL	Co-Immunoprecipitation, confocal microscopy
Venus-VAP-B	Generated *in house*	NanoBRET
EGFP-VAP-B P56S	Generated *in house*	Co-immunoprecipitation, insulin secretion
GLP-1R-NanoLuc	Generated *in house*	NanoBRET
pcDNA3.1	Addgene	Control plasmid
Dynamin1 K44A-EGFP	Addgene #34681	Co-Immunoprecipitation, confocal microscopy
Dynamin2 K44A-mRFP	Addgene #128153	Co-Immunoprecipitation, confocal microscopy
SPHKAP-EGFP	Gift from Prof John D. Scott, Howard Hughes Medical Institute[27]	Co-Immunoprecipitation, confocal microscopy
SPHKAP DFLTESE-EGFP	Generated *in house*	Co-Immunoprecipitation, confocal microscopy
pcDNA3-mitoExRai-AKAR2	Addgene #161757	Mitochondrial PKA
pcDNA3.1(+)-ExRai-AKAR2	Addgene #161753	Global PKA
cyto-Ruby3-iATPSnFR1.0	Addgene #102551	ATP
MIC19-3xHA	Gift from Prof Toshihiko Oka, Rikkyo University[68]	Immunoprecipitation, PKA-dependent phosphorylation
SPLICS Mt-ER Long P2A	Addgene #164107	Confocal microscopy
Proinsulin-NLuc	Addgene #62057	Insulin secretion

Table 1: Plasmid cDNA origin and use.

Name	Origin	Assay
Control siRNA	Ambion™ Silencer™ Select Negative Control #1 siRNA Cat#:4390843	Non-targeting Control
VAP-B siRNA	Ambion™ Silencer™ Select Pre-Designed siRNA Cat#:4390771, s133396	Co-Immunoprecipitation, insulin secretion
SPHKAP siRNA	Ambion™ Silencer™ Select Pre-Designed siRNA Cat#:4390771, s164929	Co-Immunoprecipitation, cAMP, global PKA, mitochondrial PKA, mitochondrial membrane potential, ATP, mitochondrial Morphology, insulin secretion, TUNEL, MIC19 phosphorylation

Table 2: siRNA origin and use.

Co-immunoprecipitation

INS-1 832/3 SNAP/FLAG-hGLP-1R cells were seeded in 6-well plates at $1.2x10^6$ cells per well and incubated overnight. Cells were stimulated in normal media with 100 nM exendin-4 or vehicle for 5 minutes at 37°C, washed once with cold PBS and lysed with 1 ml lysis buffer supplemented with 1% phosphatase inhibitor cocktail (Sigma-Aldrich) and 1% complete EDTA-free protease inhibitor cocktail (Sigma-Aldrich). Cell lysates were centrifuged at 12,000 g for 10 minutes, and supernatants added to 40 µl anti-FLAG M2 beads and incubated at 4°C overnight. Beads were washed three times in 500 µl wash buffer and proteins eluted with urea buffer (200 mM Tris-HCl, pH 6.8; 5% w/v SDS, 8 M urea, 100 mM dithiothreitol, 0.02% w/v bromophenol blue) at 37°C for 10 minutes before Western blot analysis.

SDS-PAGE and Western blotting

Samples were loaded on 10% SDS-polyacrylamide gels then transferred to 0.45-micron PVDF membranes and blocked with 5% skimmed milk [or 5% bovine serum albumin (BSA) for anti-phospho-PKA experiments] in TBS buffer supplemented with 0.1% Tween 20 (TBS-T). Membranes were incubated with primary antibody overnight diluted in TBS-T/milk (or TBS-T/BSA for anti-phospho-PKA antibody) at 4°C, washed in TBS-T and incubated for 1 hour at RT with HRP-conjugated secondary antibody in TBS-T/milk. Following a further 3 washes in TBS-T, membranes were developed with Clarity Western ECL substrate (BioRad) and imaged on a Biorad ChemiDoc or in a Xograph Compact X5 processor with Fuji medical X-ray films. Specific band densities were quantified in Fiji. The following antibodies were used (source, catalogue number, dilution): rabbit anti-VAP-B (Antibodies.com, A14703, 1:5,000); rabbit anti-SNAP tag (New England Biolabs, P93105, 1:5,000); mouse anti-SPHKAP (kind gift from Dr Nicholas Vierra, University of Utah[55], L131/17, 1:1,000); mouse anti-tubulin (Sigma Aldrich, T-5168, 1:2,000); rabbit anti-HA tag (Abcam, Ab9110, 1:1,000); rabbit anti-GFP (Proteintech, 50430-2-AP, 1:2,000); rabbit anti-phospho-PKA Substrate (RRXS*/T*) (Cell Signaling, 9624, 1:1,000); goat anti-mouse IgG-HRP (Abcam, ab205719, 1:5,000); goat anti-rabbit IgG HRP (Abcam, ab205718, 1:2,000).

Confocal microscopy

Cells seeded onto 35-mm glass-bottom dishes (MatTek) were transfected with the indicated constructs. SNAP-FLAG-hGLP-1R was labelled for 15 minutes at 37°C with SNAP-Surface Alexa Fluor 546 or 647 in full media prior to stimulation with 100 nM exendin-4 and imaging in a Leica Stellaris 8 inverted confocal microscope with a 63x/1.40 oil objective with Lightning confocal super resolution modality from the Facility for Imaging by Light Microscopy (FILM) at Imperial College London. For mouse islets, these were transduced 24 hours prior to imaging with an adenoviral SNAP/FLAG-hGLP-1R vector at a MOI of 1 and labelled for 10 minutes at 37°C with SNAP-Surface Alexa Fluor 647 before 5-minute stimulation with the indicated agonists and imaging of whole islets in the same microscope as above. Images were analysed in Fiji.

Electron microscopy

Cells were prepared and imaged as previously described[16]. Briefly, cells grown on Thermanox coverslips (Agar Scientific) were labelled with 2 µM cleavable SNAP-Surface biotin probe (kind gift of Dr Ivan Corrêa Jr, New England Biolabs) in full media, followed by incubation with 5 µg/ml NaN_3-free Alexa Fluor 488 Streptavidin, 10 nm colloidal gold conjugate (Molecular Probes) to label SNAP/FLAG-hGLP-1R prior to stimulation with 100 nM exendin-4, fixation and processing for conventional transmission electron microscopy (TEM), Epon stub mounting and cutting *en face* with a diamond knife (DiATOME) in a Leica Ultracut UCT ultramicrotome before examination on an FEI Tecnai

G2-Spirit TEM. Images were acquired in a charge-coupled device camera (Eagle) and analysed in Fiji.

GLP-1R – VAP-B interaction assay by NanoBRET

INS-1 832/3 cells were co-transfected with 1 µg Venus-VAP-B and 0.5 µg GLP-1R-NanoLuc. NanoBRET assay was carried out as previously described[69]. Briefly, 24 hours after transfection, cells were washed with PBS, detached, and resuspended in NanoGlo Live Cell Reagent (Promega) with furimazine (1:40 dilution in HBSS) and seeded into white 96-well half-area plates. A baseline reading was taken for 5 minutes at 37°C at 460 nm for NanoLuc emission peak and at 535 nm for Venus emission peak in a Flexstation 3 microplate reader. Cells were then stimulated with or without 1 µM of the indicated agonist and luminescent signal read for 30 minutes. Ratio (535 nm/460 nm) BRET readings were normalised to baseline readings and then normalised to average vehicle readings for agonist-specific responses. Areas under the curve (AUC) were calculated for each agonist response using GraphPad Prism 10.

Isolation and culture of pancreatic islets

Mice were humanely euthanised before inflating the pancreas through the common bile duct with RPMI-1640 medium containing 1 mg/ml collagenase (Nordmark Biochemicals). The pancreas was then dissected, incubated at 37°C for 10 minutes, and digestion halted with cold RPMI-1640 supplemented with 10% FBS (F7524, Sigma-Aldrich, UK) and 1% (v/v) penicillin/streptomycin solution (15070-063, Invitrogen). Mouse islets were subsequently washed, purified using a Histopaque gradient (Histopaque-1119 and Histopaque-1083, Sigma-Aldrich) and rested overnight at 37°C in a 95% O_2/5% CO_2 incubator before experiments in mouse culture medium as above.

Human islets received from the isolation unit at Centre Européen d'Etude du Diabète (CEED), Strasbourg, were cultured in RPMI-1640 medium supplemented with L-glutamine, 10% FBS, 1% penicillin/streptomycin solution, 0.25 µg/mL amphotericin B, and 5.5 mM glucose at 37°C in a 95% O_2/5% CO_2 incubator. Donor characteristics are indicated in Table 3.

DATE OF ARRIVAL	SEX	AGE	HEIGHT (CM)	WEIGHT (KG)	C.O.D.
14.12.23	M	34	170.18	70.8	Anoxia
29.01.24	M	71	170	86	Stroke

Table 3: Details of human islet donors.

Global and mitochondrial PKA assay

INS-1 832/3 cells were seeded onto 35-mm glass-bottom dishes (MatTek) and transfected with enhanced excitation-ratiometric PKA biosensor pcDNA3.1(+)-ExRai-AKAR2 (for global PKA) or pcDNA3-mitoExRai-AKAR2 (for mitochondrial PKA)[25]. Cells were washed with PBS 24 hours after transfection and imaged in Krebs-Ringer bicarbonate-Hepes (KRBH) buffer (140 mM NaCl, 3.6 mM KCl, 1.5 mM $CaCl_2$, 0.5 mM $MgSO_4$, 0.5 mM NaH_2PO_4, 2 mM $NaHCO_3$, 10 mM Hepes, 0.1% BSA, saturated with 95% O2/5% CO2, pH 7.4) supplemented with 11 mM glucose and imaged ratiometrically at excitation wavelengths of 405 and 488 nm and emission at 530 nm using a Zeiss LSM-780 inverted confocal laser-scanning microscope with a 63X oil objective with images taken every 6 seconds in a 37°C heated chamber. A baseline reading was taken for 1 minute followed by stimulation with 1 µM exendin-4 and imaging for 5 minutes followed by addition of 10 µM forskolin (FSK) + 100 µM

isobutyl methylxanthine (IBMX) for the last 2 minutes of acquisition. AUC were calculated using GraphPad Prism 10.

cAMP assay

INS-1 832/3 cells were seeded onto 35-mm glass-bottom dishes (MatTek) and incubated overnight with the Green Up cADDis biosensor in a BacMam vector (Montana Molecular) according to the manufacturer's instructions. Cells were washed with PBS and imaged in 11 mM glucose KRBH buffer using a Nikon Eclipse Ti microscope with an ORCA-Flash 4.0 camera (Hamamatsu) and Metamorph software (Molecular Devices) with a 20X objective and 488 nm laser with images taken every 6 seconds on a 37°C stage. A baseline reading was taken for 1 minute followed by stimulation with 1 µM exendin-4 for 5 minutes, and 10 µM FSK + 100 µM IBMX for the last 2 minutes of the acquisition. Raw fluorescent intensities were extracted in Fiji to plot an average intensity trace and AUC calculated in GraphPad Prism 10.

Mitochondrial morphology assays

INS-1 832/3 cells were seeded (50,000 cells/well) in 96-well glass-bottom imaging plates (Sigma Aldrich) coated with poly-L-lysine and laminin (1:50). Primary mouse islets were dispersed by triturating with trypsin-EDTA 0.25% for 3 minutes and seeded as above. Both cells and dispersed islets were stimulated with 100 nM exendin-4 or vehicle for 10 minutes, and subsequently labelled with MitoTracker Red CMXRos. Cells were washed once with PBS and then imaged in phenol red free RPMI-1640 in a Leica Stellaris 8 inverted confocal microscope with a 63X/1.40 oil objective. Five images were collected per well and analysed using the Mitochondria Analyzer plugin for Fiji.

Mitochondrial membrane potential assay

INS-1 832/3 cells were seeded 35-mm glass-bottom dishes (MatTek), incubated in 3 mM glucose KRBH for 1 hour, followed by incubation with 50 µM tetramethylrhodamine (TMRE) in 3 mM glucose KRBH for 15 minutes to label active mitochondria[70]. Cells were then washed with KRBH and imaged in 3 mM glucose KRBH with images taken every 12 seconds at 60X oil objective with a 561 nm laser in a Nikon Eclipse Ti microscope with an ORCA-Flash 4.0 camera (Hamamatsu) and Metamorph software (Molecular Devices). A baseline reading was recorded for 1 minute followed by stimulation with 1 µM exendin-4 in 6 mM glucose KRBH for 2 minutes. Glucose levels were then increased to 20 mM and cells imaged for 5 minutes, followed by mitochondrial hyperpolarisation using 20 µg/ml oligomycin for 5 minutes and depolarisation using 20 µM carbonyl cyanide 4-trifluoromethoxyphenylhydrazone (FCCP) for 5 minutes. Raw fluorescent intensities were extracted using Fiji to obtain average intensity traces and AUC calculated using GraphPad Prism 10.

ATP assay

INS-1 832/3 cells were seeded 35-mm glass-bottom dishes (MatTek) and transfected with the ATP biosensor cyto-Ruby3-iATPSnFR1.0[71]. Cells were imaged 24 hours after DNA transfection in 11 mM glucose KRBH in a Zeiss LSM-780 inverted confocal laser-scanning microscope at 63X oil objective with a 488 nm laser with images taken every 6 seconds. A baseline reading was recorded for 1 minute followed by stimulation with 1 µM exendin-4 for 5 minutes. Raw fluorescent intensities were extracted using Fiji to obtain average intensity traces and AUC calculated using GraphPad Prism 10.

Insulin secretion assays

INS-1 832/3 cells were seeded in 6-well plates at $1.2x10^6$ cells per well. For VAP-B WT *versus* P56S experiments, cells were co-transfected with 40 ng proinsulin-NLuc and 200 ng of either pEGFP-VAP-B, pEGFP-VAP-B-P56S or pcDNA3.1. For RNAi experiments, cells were transfected with Control *versus* Target siRNA. Cells were incubated with INS-1 832/3 media at 3 mM glucose overnight 24 hours after cDNA and 48 hours after siRNA transfections and then pre-incubated for 30 minutes in KRBH buffer supplemented with 3 mM glucose and stimulated in KRBH supplemented with 11 mM glucose with and without 100 nM exendin-4 for 60 minutes. Cell supernatants were collected to assess secreted insulin levels and cells lysed in KRBH + 0.1% Triton X100 with sonication for total insulin extraction. For cDNA-transfected cells, NanoGlo Live Cell Reagent with furimazine (1:40 dilution in HBSS) was added to samples and relative luciferase units (RLU) recorded at 460 nm using a Flexstation 3 microplate reader. For RNAi-transfected cells, samples were analysed by insulin HTRF assay (Cisbio).

TUNEL assay

INS-1 832/3 SNAP/FLAG-hGLP-1R cells seeded onto coverslips were incubated with or without 5 µM thapsigargin in either vehicle or 100 nM exendin-4 supplemented media for 8 hours before fixation and terminal deoxynucleotidyl transferase dUTP nick-end labelling (TUNEL) assay using the DeadEnd™ Fluorometric TUNEL system (Promega) following the manufacturer's instructions. Coverslips were then mounted with ProLong™ Diamond Antifade Mountant with DAPI (Thermo Fisher) and imaged for fluorescein and DAPI (to assess total cell number) in a Zeiss LSM-780 inverted confocal laser-scanning microscope at 20X objective. Percentage of TUNEL positive cells was calculated in Fiji from 5 regions per coverslip.

Proximity ligation assays

Mouse and human islets were stimulated with 100 nM exendin-4 in full media for 10 minutes at 37°C. Islets were washed with PBS and fixed for a minimum of 1 hour. Islets were washed again with PBS and processed by proximity ligation assay with the NaveniFlex Tissue MR Red kit (Navinci) following the manufacturer's instructions with an extra permeabilisation step. Antibody pairs for mouse islets were mouse anti-mouse GLP-1R Ab Mab 7F38 (DSHB) and either rabbit anti-VAP-B (A14703, Antibodies.com), or rabbit anti-mouse SPHKAP (36690, kind gift from Dr Nicholas Vierra, University of Utah[55]); antibody pairs for human islets were mouse anti-human GLP-1R Mab 3F52 (DSHB) and either rabbit anti VAP-B (A14703, Antibodies.com), or rabbit anti-human SPHKAP (HPA042499, Atlas Antibodies).

Statistical analyses for cellular experiments

All statistical analyses and graph generation was performed using GraphPad Prism 10.2.1 (GraphPad Software Inc). Statistical tests used are indicated in the corresponding figure legends. The number of replicates per comparison represents biological replicates and technical replicates within biological replicates are averaged before statistical testing. Data are presented as mean ± SEM. The p value threshold for statistical significance was set at 0.05.

Statistical analyses in human datasets

To compare the effects of *SPHKAP* gene region variants on T2D *versus* BMI, we used GWAS meta-analyses summary statistics from DIAMANTE consortium (http://www.diagram-consortium.org) for T2D by Mahajan *et al*[34], and from GIANT (https://portals.broadinstitute.org/collaboration/giant/index.php/GIANT_consortium_data_files) for BMI by Locke *et al*[37]. We report SNPs from the region surrounding *SPHKAP* gene (Chr2:228,844,666-229,046,361, NCBI human genome built37). Data pre-processing

involved merging and aligning variant effects to T2D risk-increasing allele. We extracted beta values for BMI and T2D signals and calculated respective odds ratios (OR) for T2D using the formula OR = exp(beta). The plot contains SNPs with at least nominally significant ($p<0.05$) effects on both BMI and T2D. A scatter plot was generated using RStudio with the ggplot2 package.

Acknowledgements

The authors thank Dr Nicholas Vierra, University of Utah, for the SPHKAP antibodies, Prof Toshihiko Oka, Rikkyo University, for the MIC19-3xHA construct, Prof John D. Scott, Howard Hughes Medical Institute, for the SPHKAP-EGFP construct and Dr Emily Eden, UCL, for the EGFP-VAP-B construct, as well as Imperial College FILM Facility for technical support on microscopy experiments. The AT lab is funded by grants from Diabetes UK (19/0006094), the MRC (MR/X021467/1), and the Wellcome Trust (301619/Z/23/Z). Gregory Austin is supported by a President's PhD Scholarship from Imperial College London and Affiong I. Oqua by a Commonwealth PhD Scholarship.

Main Figure Legends

Fig. 1. Exendin-4-dependent changes in β-cell GLP-1R interactome. a, Heatmap of GLP-1R interactor enrichment from anti-FLAG co-immunoprecipitates from vehicle (Veh) *versus* 5-minute exendin-4 (Ex-4)-stimulated INS-1 832/3 SNAP/FLAG-hGLP-1R cells; blue, decreased; red, increased enrichment; LC-MS/MS data analysed in LFQ-Analyst and normalised to hGLP-1R levels for each experimental sample; colour scale centred around overall median value; *n*=4. **b**, Volcano plot of data from (**a**) depicting $\log_2$ fold change to vehicle (x-axis) *versus* $-\log10_q$value (y-axis). **c**, ER, mitochondria or ERMCS-localised interactors enriched in exendin-4-stimulated *versus* vehicle conditions.

Fig. 2. Active GLP-1R binding to VAP-B. a,**b**, Co-immunoprecipitation (co-IP) of EGFP-VAP-B with hGLP-1R in vehicle (Veh) *versus* 5-minute Ex-4-stimulated INS-1 832/3 SNAP/FLAG-hGLP-1R cells. Representative blots (**a**) and quantification of EGFP-VAP-B levels per condition normalised to SNAP (**b**); *n*=3, *p<0.05 by paired t-test. **c**,**d**, As for (**a**,**b**) for endogenous VAP-B. *n*=3, *p<0.05 by paired t-test. **e**, Confocal microscopy analysis of hGLP-1R (red) co-localisation with EGFP-VAP-B (green) in Ex-4-stimulated INS-1 832/3 SNAP/FLAG-hGLP-1R cells; white box, magnification inset; size bar, 5 µm. **f**, Confocal microscopy analysis of hGLP-1R co-localisation with EGFP-VAP-B wildtype (WT), left panels, *versus* P56S, right panels, in Ex-4-stimulated INS-1 832/3 SNAP/FLAG-hGLP-1R cells; size bars, 5 µm. **g**, EGFP-VAP-B WT *versus* P56S co-IP with hGLP-1R in Veh *versus* Ex-4-stimulated INS-1 832/3 SNAP/FLAG-hGLP-1R cells. **h**, Ex-4-induced insulin secretion (fold over 11 mM glucose) in non-targeting Control *versus* VAP-B RNAi-treated INS-1 832/3 cells; *n*=4, *p<0.05 by paired t-test. **i**, Ex-4-induced insulin secretion (fold over pcDNA3.1) in EGFP-VAP-B WT- *versus* P56S-expressing INS-1 832/3 cells; *n*=5, *p<0.05 by paired t-test.

Fig. 3. Active GLP-1R binding to VAP-B requires receptor internalisation. a, Confocal microscopy analysis of hGLP-1R localisation in Ex-4-stimulated INS-1 832/3 SNAP/FLAG-hGLP-1R cells co-expressing dominant negative dynamin (Dyn) 1 and 2 K44A; white arrow indicates hGLP-1R plasma membrane localisation with Dyn1+2 K44A co-expression; yellow arrow indicates endosomal hGLP-1R localisation in a non-Dyn1+2 K44A expressing cell; size bar, 5 µm. **b**, EGFP-VAP-B co-IP with hGLP-1R in Veh *versus* Ex-4-stimulated INS-1 832/3 SNAP/FLAG-hGLP-1R cells co-expressing control pcDNA3.1 *versus* Dyn1+2 K44A. **c**, Schematic of the hGLP-1R-nanoluciferase (NLuc) – Venus-VAP-B interaction nanoBRET assay. **d**, Veh-subtracted Ex-4- *versus* exendin-F1 (Ex-F1)-induced BRET kinetic responses (left) and corresponding area under the curve (right) measuring hGLP-1R-NLuc – Venus-VAP-B interactions in INS-1 832/3 cells; *n*=3, *p<0.05 by paired t-test. **e**, Confocal microscopy analysis of hGLP-1R localisation in mouse primary islets transduced with

SNAP/FLAG-hGLP-1R adenoviruses following 5-minute stimulation with the indicated agonists [Ex-4, Ex-F1, exendin-D3 (Ex-D3), tirzepatide (Tirz) and semaglutide (Sema) used at 100 nM; orforglipron (Orf) and danuglipron (Dan) used at 5 μM]; size bars, 20 μm. **f**,**g**, EGFP-VAP-B co-IP with hGLP-1R in INS-1 832/3 SNAP/FLAG-hGLP-1R cells stimulated for 5 minutes with the indicated agonists. Representative blots (**f**) and quantification of EGFP-VAP-B levels per condition normalised to SNAP (**g**); *n*=3.

Fig. 4. Active GLP-1R localisation to ERMCSc and GLP-1R-induced mitochondrial PKA activity. a, Confocal microscopy analysis of hGLP-1R (red) co-localisation with ERMCSs (green) in Ex-4-stimulated INS-1 832/3 SNAP/FLAG-hGLP-1R cells; white box, magnification inset; size bar, 5 μm. **b**, Localisation of the excitation-ratiometric global PKA biosensor pcDNA3.1(+)- ExRai-AKAR2 in INS-1 832/3 cells; size bars,10 μm. **c**, Ex-4-stimulated global PKA response in INS-1 832/3 cells, measured with the biosensor from (**b**); Forskolin (FSK) + IBMX added for maximal response. **d**, Localisation of the excitation-ratiometric mitochondrial PKA biosensor pcDNA3-mitoExRai-AKAR2 in INS-1 832/3 cells; size bars,10 μm. **e**, Ex-4-stimulated mitochondrial PKA response in INS-1 832/3 cells, measured with the biosensor from (**d**); FSK + IBMX added for maximal response. **f**, Schematic of the AKAP SPHKAP protein primary structure. AKB, A-kinase binding domain; pFFAT, phospho-FFAT motif. Alignment of SPHKAP FFAT motif to the canonical FFAT sequence depicted; Alcoholic residues are highlighted in blue, acidic residues in green, and aromatic residues in red; all other residues are in black. **g**, Confocal microscopy analysis of SPHKAP-EGFP WT (DFLT**A**SE) *versus* FFAT domain mutant (DFLT**E**SE) localisation to mitochondria (Mitotracker Red) in INS-1 832/3 cells; size bars, 5 μm.

Fig. 5. Genetic association of *SPHKAP* variants with T2D, BMI, and random blood glucose, and VAP-B-dependent SPHKAP - GLP-1R binding. a, Comparison of the effects of *SPHKAP* gene region variants showing at least nominal association ($p<0.05$) with both T2D risk and high adiposity (BMI) from GWAS meta-analyses from Extended Data, Fig. 4b,d. X-axis [odds ratio (OR) with 95% confidence interval] corresponds to associations with T2D, while y-axis (beta with standard error) corresponds to associations with BMI. Variant points are scaled in size to their significance with T2D (z-score from association test). Seven *SPHKAP* single nucleotide polymorphisms (SNPs), 2 for T2D and 5 for high BMI, identified for T2D/BMI from GWAS Catalog (www.ebi.gwas.org) as being in high linkage disequilibrium (LD) with each other, are indicated. **b**, *SPHKAP* coding variant effects on random glucose (RG) from UKBB whole-exome sequencing (WES) data for ~450,000 individuals; y-axis represents significance ($-\log_{10}$ p-value) of variant association and x-axis represents the genomic location of variants (NCBI human genome build37). Secondary y-axis represents recombination fraction from 1000 Genomes Project and horizontal dashed line highlights the association threshold for significance ($p=5\times10^{-8}$). RG levels in mmol/l are natural logarithm transformed and adjusted for time since last meal (t) as $t+t^2+t^3$, age, sex, and six principal components (derived from UKBB GWAS data). **c**, Endogenous SPHKAP co-IP with hGLP-1R in Veh *versus* Ex-4-stimulated INS-1 832/3 SNAP/FLAG-hGLP-1R cells. **d**, SPHKAP-EGFP co-IP with hGLP-1R in non-targeting Control *versus* VAP-B RNAi-treated INS-1 832/3 SNAP/FLAG-hGLP-1R cells under Veh *versus* Ex-4-stimulated conditions. **e**, SPHKAP-EGFP FFAT domain mutant (DFLT**E**SE) co-IP with hGLP-1R in Veh *versus* Ex-4-stimulated INS-1 832/3 SNAP/FLAG-hGLP-1R cells.

Fig. 6. Role of SPHKAP in GLP-1R-dependent mitochondrial function and morphology. a, Ex-4-stimulated mitochondrial PKA responses in Control *versus* SPHKAP RNAi-treated INS-1 832/3 cells. Left: PKA traces; right: AUC quantification; *n*=4, *p<0.05 by paired t-test. **b**, Ex-4-stimulated changes in mitochondrial membrane potential in Control *versus* SPHKAP RNAi-treated INS-1 832/3 cells, measured with TMRE. Left: membrane potential traces; G20, 20 mM glucose. Right: Quantification of Ex-4 and G20 AUC; *n*=5, *p<0.05 by paired t-test. **c**, Ex-4-stimulated ATP responses in Control *versus* SPHKAP RNAi-treated INS-1 832/3 cells, measured with the cyto- Ruby3-iATPSnFR1.0 biosensor. Left: ATP traces. Right: AUC

quantification; *n*=3, *p<0.05 by paired t-test. **d**,**e**, PKA-dependent phosphorylation of MIC19-3xHA in INS-1 832/3 cells under Veh *versus* Ex-4-stimulated conditions, determined by Western blotting of anti-HA immunoprecipitates with an anti-RRx-pS/T antibody. FSK, positive control for PKA activation. Representative blots (**d**) and quantification of phospho-MIC19 levels per condition (**e**); *n*=3, *p<0.05 by one-way ANOVA with Šidák post-hoc test. **f**, PKA-dependent phosphorylation of MIC19-3xHA in Control *versus* SPHKAP or VAP-B RNAi-treated INS-1 832/3 cells under Veh *versus* Ex-4-stimulated conditions. **g**,**h**, Confocal microscopy analysis of mitochondrial morphology in Control *versus* SPHKAP RNAi-treated INS-1 832/3 cells under Veh *versus* Ex-4-stimulated conditions; MitoTracker Red staining (**g**) and quantification of mitochondrial mean form factor and mean area (**h**); *n*=5, *p<0.05, **p<0.01 by one-way ANOVA with Šidák post-hoc test.

Fig. 7. Role of SPHKAP in GLP-1R control of β-cell function. a, Ex-4-induced insulin secretion (fold over 11 mM glucose) in non-targeting Control *versus* SPHKAP RNAi-treated INS-1 832/3 cells; *n*=3, *p<0.05 by paired t-test. **b**, Percentage of apoptosis with and without thapsigargin exposure in Control *versus* SPHKAP RNAi-treated INS-1 832/3 cells under Veh *versus* Ex-4-stimulated conditions; *n*=3; *p<0.05 by one-way ANOVA with Šidák post-hoc test.

Fig. 8. Endogenous GLP-1R interaction with VAP-B and SPHKAP and mitochondrial effects in primary islets. a, Proximity ligation assays (PLA) representative images showing interactions between endogenous GLP-1R and VAP-B (left) or SPHKAP (right) in Ex-4-stimulated primary mouse islets; size bars, 20 µm. **b**, As in (**a**) for primary human islets. **c**,**d**, Confocal microscopy analysis of mitochondrial morphology in Control *versus* SPHKAP RNAi-treated dispersed mouse islets under Veh *versus* Ex-4-stimulated conditions; MitoTracker Red staining (**c**) and quantification of mitochondrial mean form factor and mean area (**d**); *n*=4, *p<0.05 by one-way ANOVA with Šidák post-hoc test.

Extended Figure Legends

Extended Data Fig. 1. Interactome analysis of GLP-1R binding partners in pancreatic β-cells – Extra data. a, Principal component analysis (PCA) of biological repeats from interactome data from Fig. 1. **b**, Pathway enrichment analysis using gProfiler; results show 10 most significant gene ontology terms represented in the interactome data from Fig.1.

Extended Data Fig. 2. Active GLP-1R binding to VAP-B – Extra data. a, Electron microscopy micrograph depicting gold-labelled hGLP-1R (arrows) localised to an endosome – ER MCS in Ex-4-stimulated INS-1 832/3 SNAP/FLAG-hGLP-1R cells; Endosome highlighted in gold and ER in blue; size bar, 100 nm. **b**,**c**, Western blot analysis of endogenous VAP-B levels in Control *versus* VAP-B RNAi-treated INS-1 832/3 cells; representative blots (**b**) and quantification of VAP-B knockdown (**c**); *n*=3, **p<0.01 by paired t-test.

Extended Data Fig. 3. Interactome analysis of GLP-1R binding partners in pancreatic β-cells - Further agonists. Heatmap of GLP-1R interactor enrichment from anti-FLAG co-immunoprecipitates from INS-1 832/3 SNAP/FLAG-hGLP-1R cells stimulated for 5 minutes with the indicated agonists; blue, decreased; red, increased enrichment; LC-MS/MS data analysed in LFQ-Analyst and normalised to hGLP-1R levels for each experimental sample; colour scale centred around overall median value; *n*=4 for Ex-4, Ex-F1 and Ex-D3 and *n*=3 for GLP-1.

Extended Data Fig. 4. Gene expression data and genetic association of *SPHKAP* variants with T2D and BMI – Extra data. a, Analysis of *SPHKAP* mRNA levels from primary islets isolated from WT *versus* heterozygous and homozygous *db*/*db* mice; data

obtained from RNA Seq dataset GSE107489[72]; *n*=3, **p<0.01 by one-way ANOVA with Dunnett post-hoc test. **b**,**c**, *SPHKAP* gene region variant associations from T2D European ancestry (**b**)[34] and T2D all ancestries (**c**)[35] GWAS; y-axes represent significance ($-\log_{10}$ p-value) of phenotype – variant associations and x-axes genomic location of the variants (NCBI human genome build37). Secondary y-axes represent recombination fraction from 1000 Genomes Project and horizontal dashed lines highlight association threshold for significance ($p=5\times10^{-8}$). Lead variant with the highest significance is shown as a purple diamond and correlation (LD, r^2) of other SNPs in the lead variant region represented with colours as per box legend (**b**). Variants previously reported for associations with phenotypes in GWAS catalog (www.ebi.gwas.org) are indicated and respective phenotypes listed. **d**,**e**, As for (**b**,**c**) for BMI GWAS meta-analyses[36, 37].

Extended Data Fig. 5. Role of SPHKAP in GLP-1R-dependent mitochondrial function and morphology – Extra data. a, Western blot analysis of endogenous SPHKAP levels in Control *versus* SPHKAP RNAi-treated INS-1 832/3 cells. **b**, Western blot analysis of SPHKAP-EGFP levels in Control *versus* SPHKAP RNAi-treated INS-1 832/3 cells. **c**, EGFP-VAP-B co-IP with hGLP-1R in Control *versus* SPHKAP RNAi-treated INS-1 832/3 SNAP/FLAG-hGLP-1R cells under Veh *versus* Ex-4-stimulated conditions. **d**, Confocal microscopy analysis of EGFP-VAP-B co-localisation with hGLP-1R in Ex-4-stimulated Control *versus* SPHKAP RNAi-treated INS-1 832/3 SNAP/FLAG-hGLP-1R cells; size bars, 5 µm. **e**, Ex-4-stimulated cAMP responses in Control *versus* SPHKAP RNAi-treated INS-1 832/3 cells, measured with the cADDis cAMP biosensor. Left: cAMP traces; right: AUC quantification; *n*=3, non-significant (ns) by paired t-test. **f**, Ex-4-stimulated global PKA responses in Control *versus* SPHKAP RNAi-treated INS-1 832/3 cells. Left: PKA traces; right: AUC quantification; *n*=4, ns by paired t-test.

Extended Data Fig. 6. Endogenous GLP-1R interaction with VAP-B and SPHKAP – Extra data. Negative controls (no primary antibody) for PLA data shown in Fig. 8.

References

1. Rivera Nieves, A.M., Wauford, B.M. & Fu, A. Mitochondrial bioenergetics, metabolism, and beyond in pancreatic β-cells and diabetes. *Frontiers in Molecular Biosciences* **11** (2024).
2. Haythorne, E. *et al.* Diabetes causes marked inhibition of mitochondrial metabolism in pancreatic beta-cells. *Nat Commun* **10**, 2474 (2019).
3. Rivera Nieves, A.M., Wauford, B.M. & Fu, A. Mitochondrial bioenergetics, metabolism, and beyond in pancreatic beta-cells and diabetes. *Front Mol Biosci* **11**, 1354199 (2024).
4. Ahmad, E., Lim, S., Lamptey, R., Webb, D.R. & Davies, M.J. Type 2 diabetes. *Lancet* **400**, 1803-1820 (2022).
5. Mayendraraj, A., Rosenkilde, M.M. & Gasbjerg, L.S. GLP-1 and GIP receptor signaling in beta cells - A review of receptor interactions and co-stimulation. *Peptides* **151**, 170749 (2022).
6. Boland, M.L. *et al.* Resolution of NASH and hepatic fibrosis by the GLP-1R/GcgR dual-agonist Cotadutide via modulating mitochondrial function and lipogenesis. *Nat Metab* **2**, 413-431 (2020).
7. Timper, K. *et al.* GLP-1 Receptor Signaling in Astrocytes Regulates Fatty Acid Oxidation, Mitochondrial Integrity, and Function. *Cell Metab* **31**, 1189-1205 e1113 (2020).
8. Wu, P. *et al.* Liraglutide Regulates Mitochondrial Quality Control System Through PGC-1alpha in a Mouse Model of Parkinson's Disease. *Neurotox Res* **40**, 286-297 (2022).
9. Carlessi, R. *et al.* GLP-1 receptor signalling promotes beta-cell glucose metabolism via mTOR-dependent HIF-1alpha activation. *Sci Rep* **7**, 2661 (2017).

10. Ng, M.Y.W., Wai, T. & Simonsen, A. Quality control of the mitochondrion. *Dev Cell* **56**, 881-905 (2021).
11. Prinz, W.A., Toulmay, A. & Balla, T. The functional universe of membrane contact sites. *Nat Rev Mol Cell Biol* **21**, 7-24 (2020).
12. Dudas, E.F., Huynen, M.A., Lesk, A.M. & Pastore, A. Invisible leashes: The tethering VAPs from infectious diseases to neurodegeneration. *J Biol Chem* **296**, 100421 (2021).
13. Kors, S., Costello, J.L. & Schrader, M. VAP Proteins - From Organelle Tethers to Pathogenic Host Interactors and Their Role in Neuronal Disease. *Front Cell Dev Biol* **10**, 895856 (2022).
14. Suzuki, H. *et al.* ALS-linked P56S-VAPB, an aggregated loss-of-function mutant of VAPB, predisposes motor neurons to ER stress-related death by inducing aggregation of co-expressed wild-type VAPB. *J Neurochem* **108**, 973-985 (2009).
15. Obara, C.J. *et al.* Motion of VAPB molecules reveals ER-mitochondria contact site subdomains. *Nature* **626**, 169-176 (2024).
16. Jones, B. *et al.* Targeting GLP-1 receptor trafficking to improve agonist efficacy. *Nat Commun* **9**, 1602 (2018).
17. Fang, Z. *et al.* Ligand-Specific Factors Influencing GLP-1 Receptor Post-Endocytic Trafficking and Degradation in Pancreatic Beta Cells. *Int J Mol Sci* **21** (2020).
18. Madsbad, S. & Holst, J.J. Glycaemic control and weight loss with semaglutide in type 2 diabetes. *Lancet Diabetes Endocrinol* **5**, 315-317 (2017).
19. Nauck, M.A. & D'Alessio, D.A. Tirzepatide, a dual GIP/GLP-1 receptor co-agonist for the treatment of type 2 diabetes with unmatched effectiveness regrading glycaemic control and body weight reduction. *Cardiovasc Diabetol* **21**, 169 (2022).
20. Dutta, D. *et al.* Orforglipron, a novel non-peptide oral daily glucagon-like peptide-1 receptor agonist as an anti-obesity medicine: A systematic review and meta-analysis. *Obes Sci Pract* **10**, e743 (2024).
21. Fatima, H. *et al.* Evaluating Glycemic Control Efficacy and Safety of the Oral Small Molecule Glucagon-Like Peptide 1 Receptor Agonist Danuglipron in Type 2 Diabetes Patients: A Systemic Review and Meta-Analysis. *Diabetes Metab Syndr Obes* **16**, 3567-3578 (2023).
22. Novikoff, A. *et al.* Spatiotemporal GLP-1 and GIP receptor signaling and trafficking/recycling dynamics induced by selected receptor mono- and dual-agonists. *Mol Metab* **49**, 101181 (2021).
23. Vallese, F. *et al.* An expanded palette of improved SPLICS reporters detects multiple organelle contacts in vitro and in vivo. *Nat Commun* **11**, 6069 (2020).
24. Akabane, S. & Oka, T. Insights into the regulation of mitochondrial functions by protein kinase A-mediated phosphorylation. *J Biochem* **175**, 1-7 (2023).
25. Zhang, J.F. *et al.* An ultrasensitive biosensor for high-resolution kinase activity imaging in awake mice. *Nat Chem Biol* **17**, 39-46 (2021).
26. Kovanich, D. *et al.* Sphingosine kinase interacting protein is an A-kinase anchoring protein specific for type I cAMP-dependent protein kinase. *Chembiochem* **11**, 963-971 (2010).
27. Means, C.K. *et al.* An entirely specific type I A-kinase anchoring protein that can sequester two molecules of protein kinase A at mitochondria. *Proc Natl Acad Sci U S A* **108**, E1227-1235 (2011).
28. Deng, Z. *et al.* Selective autophagy of AKAP11 activates cAMP/PKA to fuel mitochondrial metabolism and tumor cell growth. *Proc Natl Acad Sci U S A* **118** (2021).
29. Neefjes, J. & Cabukusta, B. What the VAP: The Expanded VAP Family of Proteins Interacting With FFAT and FFAT-Related Motifs for Interorganellar Contact. *Contact (Thousand Oaks)* **4**, 25152564211012246 (2021).
30. Di Mattia, T. *et al.* FFAT motif phosphorylation controls formation and lipid transfer function of inter-organelle contacts. *EMBO J* **39**, e104369 (2020).

31. Loewen, C.J., Roy, A. & Levine, T.P. A conserved ER targeting motif in three families of lipid binding proteins and in Opi1p binds VAP. *EMBO J* **22**, 2025-2035 (2003).
32. Wang, Y., Harashima, S.I., Liu, Y., Usui, R. & Inagaki, N. Sphingosine kinase 1-interacting protein is a novel regulator of glucose-stimulated insulin secretion. *Sci Rep* **7**, 779 (2017).
33. Liu, Y. *et al.* Sphingosine kinase 1-interacting protein is a dual regulator of insulin and incretin secretion. *FASEB J* **33**, 6239-6253 (2019).
34. Mahajan, A. *et al.* Multi-ancestry genetic study of type 2 diabetes highlights the power of diverse populations for discovery and translation. *Nat Genet* **54**, 560-572 (2022).
35. Suzuki, K. *et al.* Genetic drivers of heterogeneity in type 2 diabetes pathophysiology. *Nature* **627**, 347-357 (2024).
36. Pulit, S.L. *et al.* Meta-analysis of genome-wide association studies for body fat distribution in 694 649 individuals of European ancestry. *Hum Mol Genet* **28**, 166-174 (2019).
37. Locke, A.E. *et al.* Genetic studies of body mass index yield new insights for obesity biology. *Nature* **518**, 197-206 (2015).
38. Friedman, J.R., Mourier, A., Yamada, J., McCaffery, J.M. & Nunnari, J. MICOS coordinates with respiratory complexes and lipids to establish mitochondrial inner membrane architecture. *Elife* **4** (2015).
39. Dong, J. *et al.* Mic19 depletion impairs endoplasmic reticulum-mitochondrial contacts and mitochondrial lipid metabolism and triggers liver disease. *Nat Commun* **15**, 168 (2024).
40. Pearson, R.B. & Kemp, B.E. Protein kinase phosphorylation site sequences and consensus specificity motifs: tabulations. *Methods Enzymol* **200**, 62-81 (1991).
41. Bock-Bierbaum, T. *et al.* Structural insights into crista junction formation by the Mic60-Mic19 complex. *Sci Adv* **8**, eabo4946 (2022).
42. Ast, J. *et al.* Revealing the tissue-level complexity of endogenous glucagon-like peptide-1 receptor expression and signaling. *Nat Commun* **14**, 301 (2023).
43. Ast, J. *et al.* Expanded LUXendin Color Palette for GLP1R Detection and Visualization In Vitro and In Vivo. *JACS Au* **2**, 1007-1017 (2022).
44. Ast, J., Broichhagen, J. & Hodson, D.J. Reagents and models for detecting endogenous GLP1R and GIPR. *EBioMedicine* **74**, 103739 (2021).
45. Veluthakal, R. *et al.* Mitochondrial Dysfunction, Oxidative Stress, and Inter-Organ Miscommunications in T2D Progression. *Int J Mol Sci* **25** (2024).
46. Rutter, G.A., Sidarala, V., Kaufman, B.A. & Soleimanpour, S.A. Mitochondrial metabolism and dynamics in pancreatic beta cell glucose sensing. *Biochem J* **480**, 773-789 (2023).
47. Koeck, T. *et al.* A common variant in TFB1M is associated with reduced insulin secretion and increased future risk of type 2 diabetes. *Cell Metab* **13**, 80-91 (2011).
48. Reardon, W. *et al.* Diabetes mellitus associated with a pathogenic point mutation in mitochondrial DNA. *Lancet* **340**, 1376-1379 (1992).
49. Mulder, H. Transcribing beta-cell mitochondria in health and disease. *Mol Metab* **6**, 1040-1051 (2017).
50. Anton, S.E. *et al.* Receptor-associated independent cAMP nanodomains mediate spatiotemporal specificity of GPCR signaling. *Cell* **185**, 1130-1142 e1111 (2022).
51. Xie, B., Nguyen, P.M. & Idevall-Hagren, O. Feedback regulation of insulin secretion by extended synaptotagmin-1. *FASEB J* **33**, 4716-4728 (2019).
52. Xie, B. *et al.* The endoplasmic reticulum-plasma membrane tethering protein TMEM24 is a regulator of cellular Ca2+ homeostasis. *J Cell Sci* **135** (2022).
53. Panagiotou, S. *et al.* OSBP-mediated PI(4)P-cholesterol exchange at endoplasmic reticulum-secretory granule contact sites controls insulin secretion. *Cell Rep* **43**, 113992 (2024).
54. Han, J. *et al.* The Identification of Novel Protein-Protein Interactions in Liver that Affect Glucagon Receptor Activity. *PLoS One* **10**, e0129226 (2015).

55. Vierra, N.C. *et al.* Neuronal ER-plasma membrane junctions couple excitation to Ca(2+)-activated PKA signaling. *Nat Commun* **14**, 5231 (2023).
56. Xie, Y. *et al.* GLP-1 improves the neuronal supportive ability of astrocytes in Alzheimer's disease by regulating mitochondrial dysfunction via the cAMP/PKA pathway. *Biochem Pharmacol* **188**, 114578 (2021).
57. Paradies, G., Paradies, V., Ruggiero, F.M. & Petrosillo, G. Role of Cardiolipin in Mitochondrial Function and Dynamics in Health and Disease: Molecular and Pharmacological Aspects. *Cells* **8** (2019).
58. Zhang, J. & Shi, Y. In Search of the Holy Grail: Toward a Unified Hypothesis on Mitochondrial Dysfunction in Age-Related Diseases. *Cells* **11** (2022).
59. Hugenroth, M. & Bohnert, M. Come a little bit closer! Lipid droplet-ER contact sites are getting crowded. *Biochim Biophys Acta Mol Cell Res* **1867**, 118603 (2020).
60. Prentki, M., Peyot, M.L., Masiello, P. & Madiraju, S.R.M. Nutrient-Induced Metabolic Stress, Adaptation, Detoxification, and Toxicity in the Pancreatic beta-Cell. *Diabetes* **69**, 279-290 (2020).
61. Sassano, M.L., Felipe-Abrio, B. & Agostinis, P. ER-mitochondria contact sites; a multifaceted factory for Ca(2+) signaling and lipid transport. *Front Cell Dev Biol* **10**, 988014 (2022).
62. Raffaello, A., Mammucari, C., Gherardi, G. & Rizzuto, R. Calcium at the Center of Cell Signaling: Interplay between Endoplasmic Reticulum, Mitochondria, and Lysosomes. *Trends Biochem Sci* **41**, 1035-1049 (2016).
63. Sharma, A.K., Khandelwal, R. & Wolfrum, C. Futile cycles: Emerging utility from apparent futility. *Cell Metab* (2024).
64. Naylor, J. *et al.* Use of CRISPR/Cas9-engineered INS-1 pancreatic beta cells to define the pharmacology of dual GIPR/GLP-1R agonists. *Biochem J* **473**, 2881-2891 (2016).
65. Yu, V. *et al.* Differential CpG methylation at Nnat in the early establishment of beta cell heterogeneity. *Diabetologia* (2024).
66. Tyanova, S., Temu, T. & Cox, J. The MaxQuant computational platform for mass spectrometry-based shotgun proteomics. *Nat Protoc* **11**, 2301-2319 (2016).
67. Shah, A.D., Goode, R.J.A., Huang, C., Powell, D.R. & Schittenhelm, R.B. LFQ-Analyst: An Easy-To-Use Interactive Web Platform To Analyze and Visualize Label-Free Proteomics Data Preprocessed with MaxQuant. *J Proteome Res* **19**, 204-211 (2020).
68. Akabane, S. *et al.* PKA Regulates PINK1 Stability and Parkin Recruitment to Damaged Mitochondria through Phosphorylation of MIC60. *Mol Cell* **62**, 371-384 (2016).
69. Manchanda, Y. *et al.* Enhanced Endosomal Signaling and Desensitization of GLP-1R vs GIPR in Pancreatic Beta Cells. *Endocrinology* **164** (2023).
70. Perry, S.W., Norman, J.P., Barbieri, J., Brown, E.B. & Gelbard, H.A. Mitochondrial membrane potential probes and the proton gradient: a practical usage guide. *Biotechniques* **50**, 98-115 (2011).
71. Lobas, M.A. *et al.* A genetically encoded single-wavelength sensor for imaging cytosolic and cell surface ATP. *Nat Commun* **10**, 711 (2019).
72. Neelankal John, A., Ram, R. & Jiang, F.X. RNA-Seq Analysis of Islets to Characterise the Dedifferentiation in Type 2 Diabetes Model Mice db/db. *Endocr Pathol* **29**, 207-221 (2018).

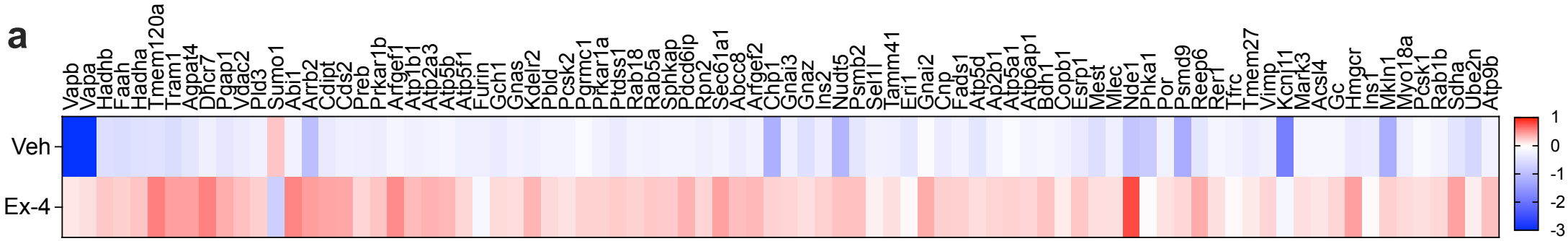

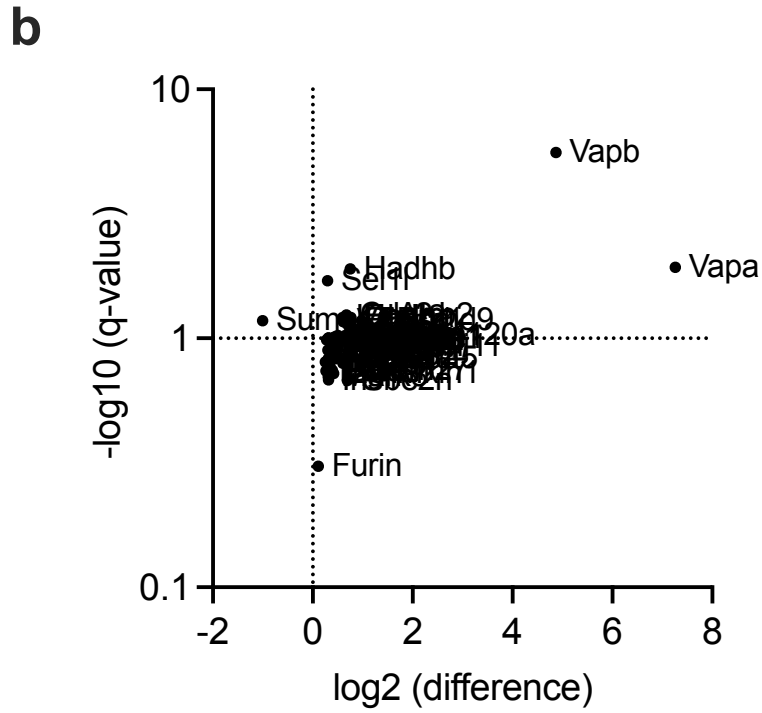

c

Name	Localisation	Function
VAPB	ER-Mitochondria contacts	lipid and ion transport
VAPA	ER-Mitochondria contacts	lipid and ion transport
HADHB	Mitochondria	β-oxidation of long chain fatty acids
FAAH	ER-Mitochondria contacts	fatty acid amide hydrolysis
HADHA	Mitochondria	β-oxidation of long chain fatty acids
APGAT4	ER / Mitochondria	phosphatidic acid biosynthesis
DHCR7	ER	cholesterol biosynthesis
VDAC2	ER-Mitochondria contacts	metabolite transport, mPTP component
CDS2	ER	phosphatidylinositol biosynthesis
ATP2A3	ER-Mitochondria contacts	SERCA pump, calcium transport
ATP5B	Mitochondria	ATP synthase subunit
ATP5F1	Mitochondria	ATP synthase subunit
PGRMC1	ER / Mitochondria	cholesterol metabolism
PTDSS1	ER	phosphatidylserine biosynthesis
Rab18	ER	lipid droplet biogenesis, lipolysis
SPHKAP	Mitochondria	PKA anchoring protein
TAMM41	Mitochondria	phosphatidylinositol biosynthesis
CNP	Mitochondria	calcium-induced opening of mPTP
FADS1	Mitochondria	fatty acid unsaturation
ATP5D	Mitochondria	ATP synthase subunit
ATP5A1	Mitochondria	ATP synthase subunit
BDH1	Mitochondria	fatty acid catabolism
POR	ER	cholesterol biosynthesis
REEP6	ER-Mitochondria contacts	GPCR regulation of mitochondrial function
HMGCR	ER	cholesterol biosynthesis
SDHA	Mitochondria	mitochondrial respiratory chain complex

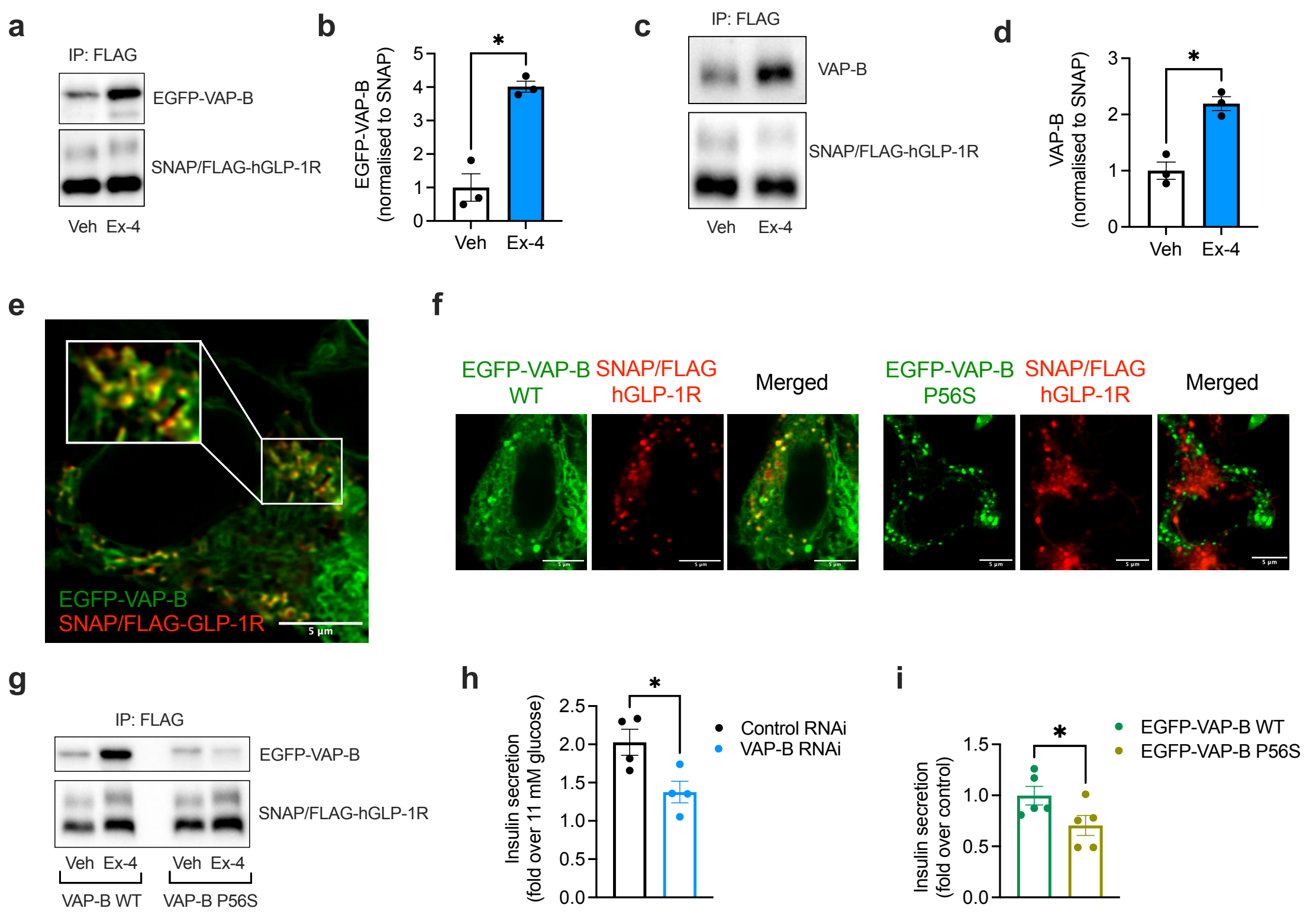
a
IP: FLAG
EGFP-VAP-B
SNAP/FLAG-hGLP-1R
Veh Ex-4
b
EGFP-VAP-B (normalised to SNAP)
0
1
2
3
4
5
*
Veh
Ex-4
c
IP: FLAG
VAP-B
SNAP/FLAG-hGLP-1R
Veh
Ex-4
d
VAP-B (normalised to SNAP)
0
1
2
3
*
Veh
Ex-4
e
EGFP-VAP-B
SNAP/FLAG-GLP-1R
5 µm
f
EGFP-VAP-B WT
SNAP/FLAG hGLP-1R
Merged
EGFP-VAP-B P56S
SNAP/FLAG hGLP-1R
Merged
g
IP: FLAG
EGFP-VAP-B
SNAP/FLAG-hGLP-1R
Veh Ex-4
Veh Ex-4
VAP-B WT
VAP-B P56S
h
Insulin secretion (fold over 11 mM glucose)
0.0
0.5
1.0
1.5
2.0
2.5
*
Control RNAi
VAP-B RNAi
i
Insulin secretion (fold over control)
0.0
0.5
1.0
1.5
*
EGFP-VAP-B WT
EGFP-VAP-B P56S

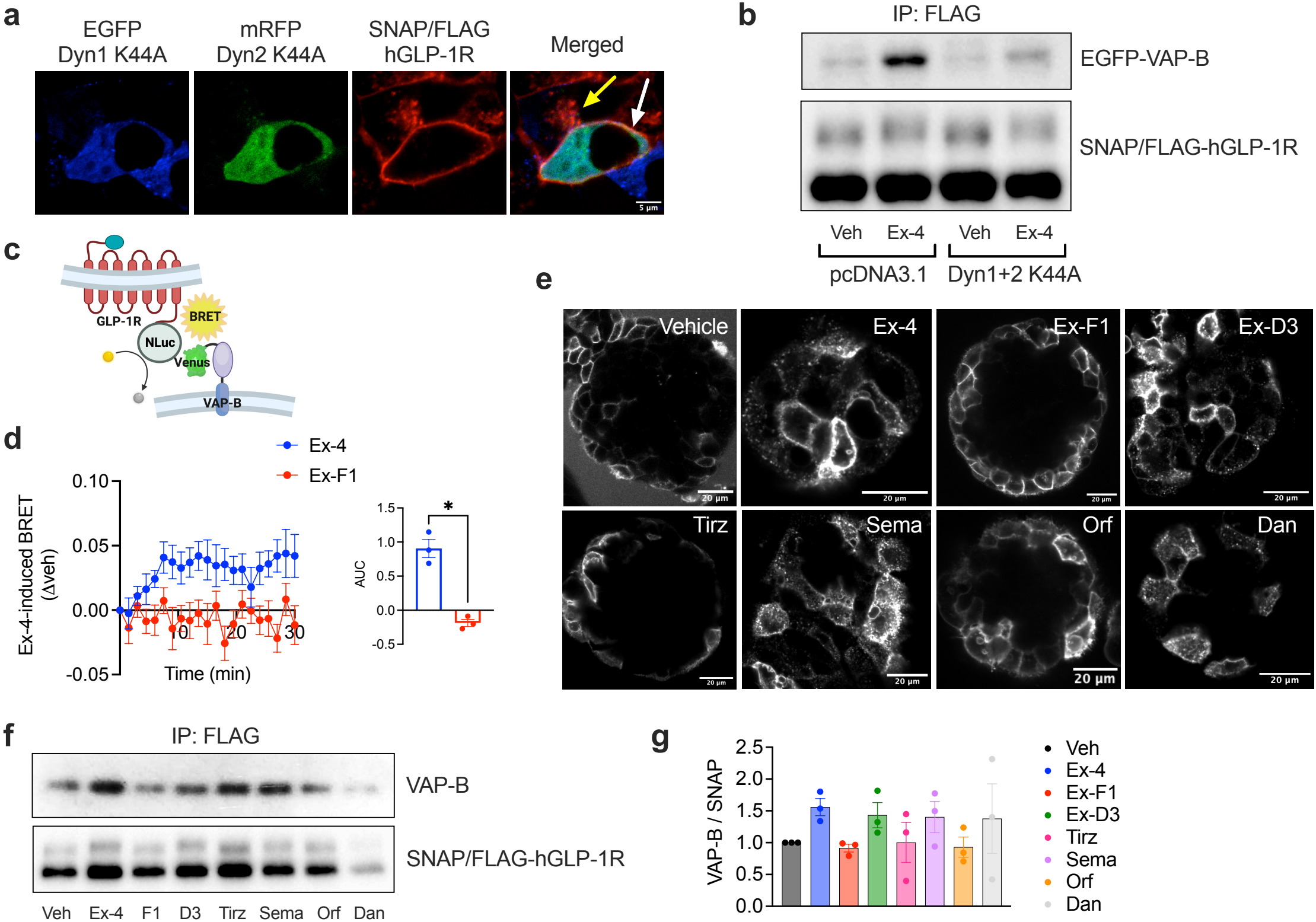
a
EGFP Dyn1 K44A
mRFP Dyn2 K44A
SNAP/FLAG hGLP-1R
Merged
5 µm
b
IP: FLAG
EGFP-VAP-B
SNAP/FLAG-hGLP-1R
Veh
Ex-4
Veh
Ex-4
pcDNA3.1
Dyn1+2 K44A
c
GLP-1R
BRET
NLuc
Venus
VAP-B
d
Ex-4
Ex-F1
Ex-4-induced BRET (Δveh)
0.10
0.05
0.00
-0.05
10
20
30
Time (min)
AUC
1.5
1.0
0.5
0.0
-0.5
*
e
Vehicle
Ex-4
Ex-F1
Ex-D3
Tirz
Sema
Orf
Dan
20 µm
f
IP: FLAG
VAP-B
SNAP/FLAG-hGLP-1R
Veh
Ex-4
F1
D3
Tirz
Sema
Orf
Dan
g
VAP-B / SNAP
2.5
2.0
1.5
1.0
0.5
0.0
Veh
Ex-4
Ex-F1
Ex-D3
Tirz
Sema
Orf
Dan

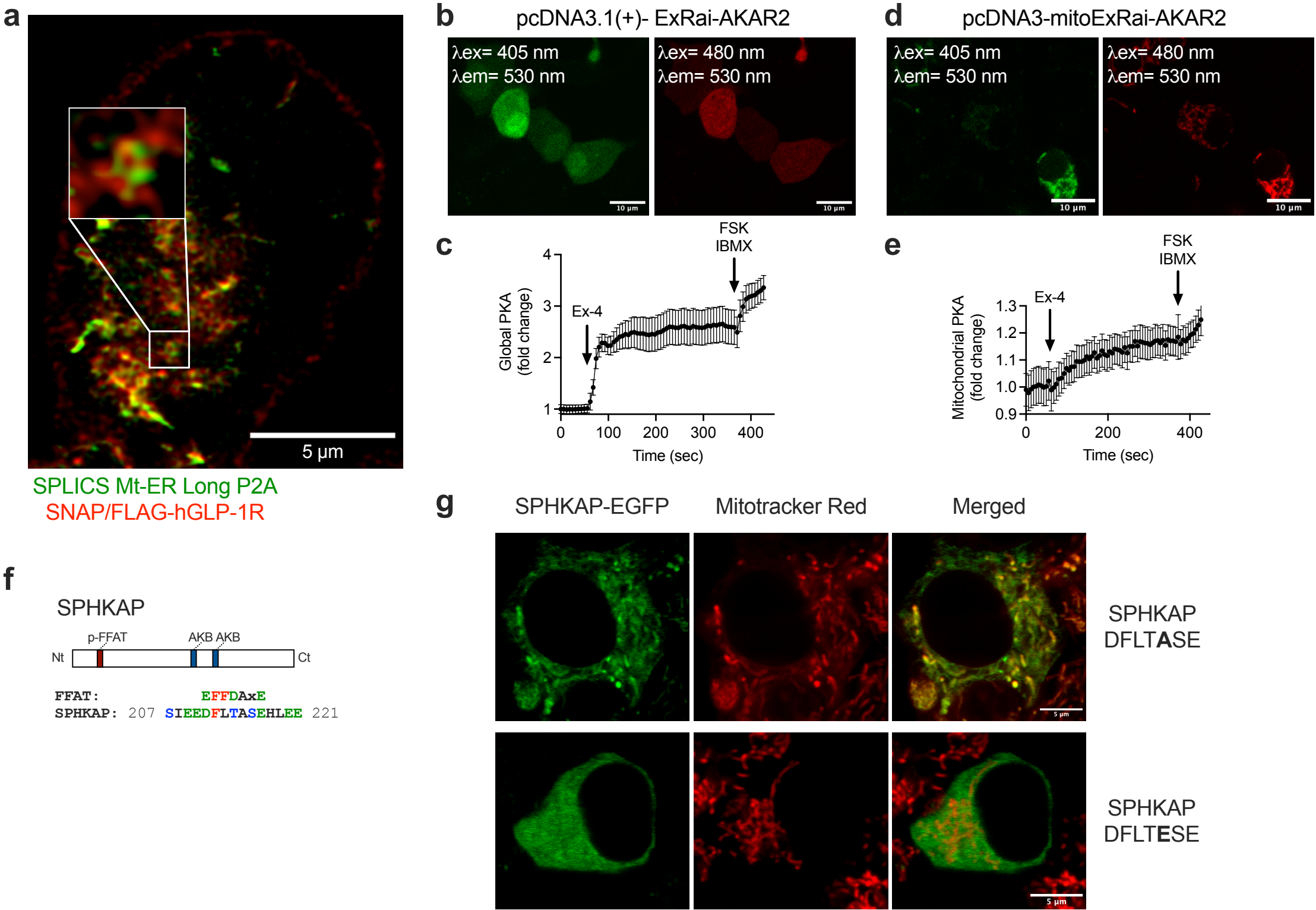
a
5 µm
SPLICS Mt-ER Long P2A
SNAP/FLAG-hGLP-1R
b
pcDNA3.1(+)- ExRai-AKAR2
λex= 405 nm
λem= 530 nm
λex= 480 nm
λem= 530 nm
10 µm
d
pcDNA3-mitoExRai-AKAR2
λex= 405 nm
λem= 530 nm
λex= 480 nm
λem= 530 nm
10 µm
c
Global PKA (fold change)
Ex-4
FSK
IBMX
Time (sec)
e
Mitochondrial PKA (fold change)
Ex-4
FSK
IBMX
Time (sec)
f
SPHKAP
p-FFAT
AKB AKB
Nt
Ct
FFAT: EFFDAxE
SPHKAP: 207 SIEEDFLTASEHLEE 221
g
SPHKAP-EGFP
Mitotracker Red
Merged
SPHKAP DFLTASE
SPHKAP DFLTESE
5 µm

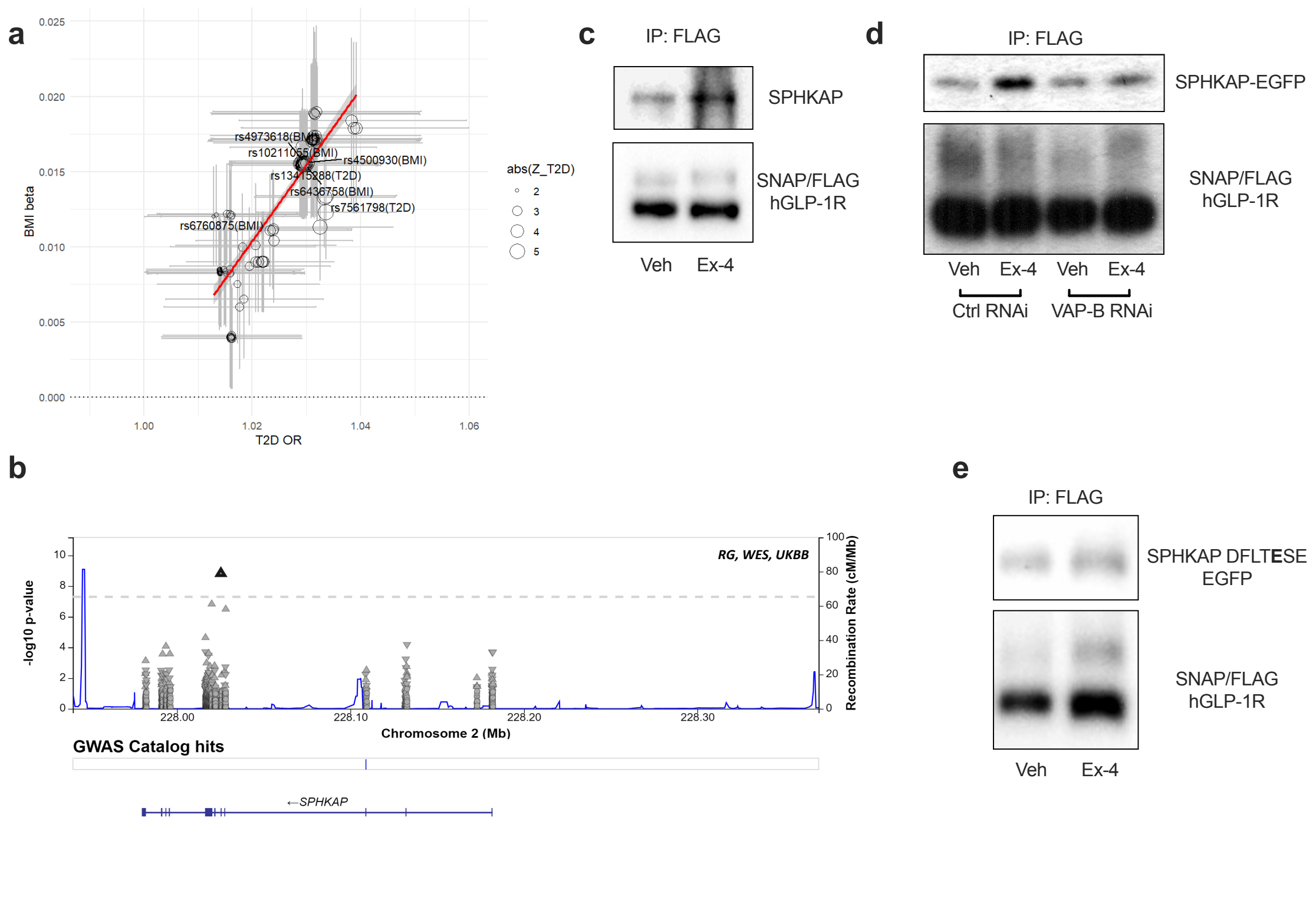
a
BMI beta
T2D OR
rs4973618(BMI)
rs10211055(BMI)
rs4500930(BMI)
rs13415288(T2D)
rs6436758(BMI)
rs7561798(T2D)
rs6760875(BMI)
abs(Z_T2D)
2
3
4
5
b
-log10 p-value
Recombination Rate (cM/Mb)
RG, WES, UKBB
Chromosome 2 (Mb)
GWAS Catalog hits
←SPHKAP
c
IP: FLAG
SPHKAP
SNAP/FLAG hGLP-1R
Veh
Ex-4
d
IP: FLAG
SPHKAP-EGFP
SNAP/FLAG hGLP-1R
Veh
Ex-4
Veh
Ex-4
Ctrl RNAi
VAP-B RNAi
e
IP: FLAG
SPHKAP DFLTESE EGFP
SNAP/FLAG hGLP-1R
Veh
Ex-4

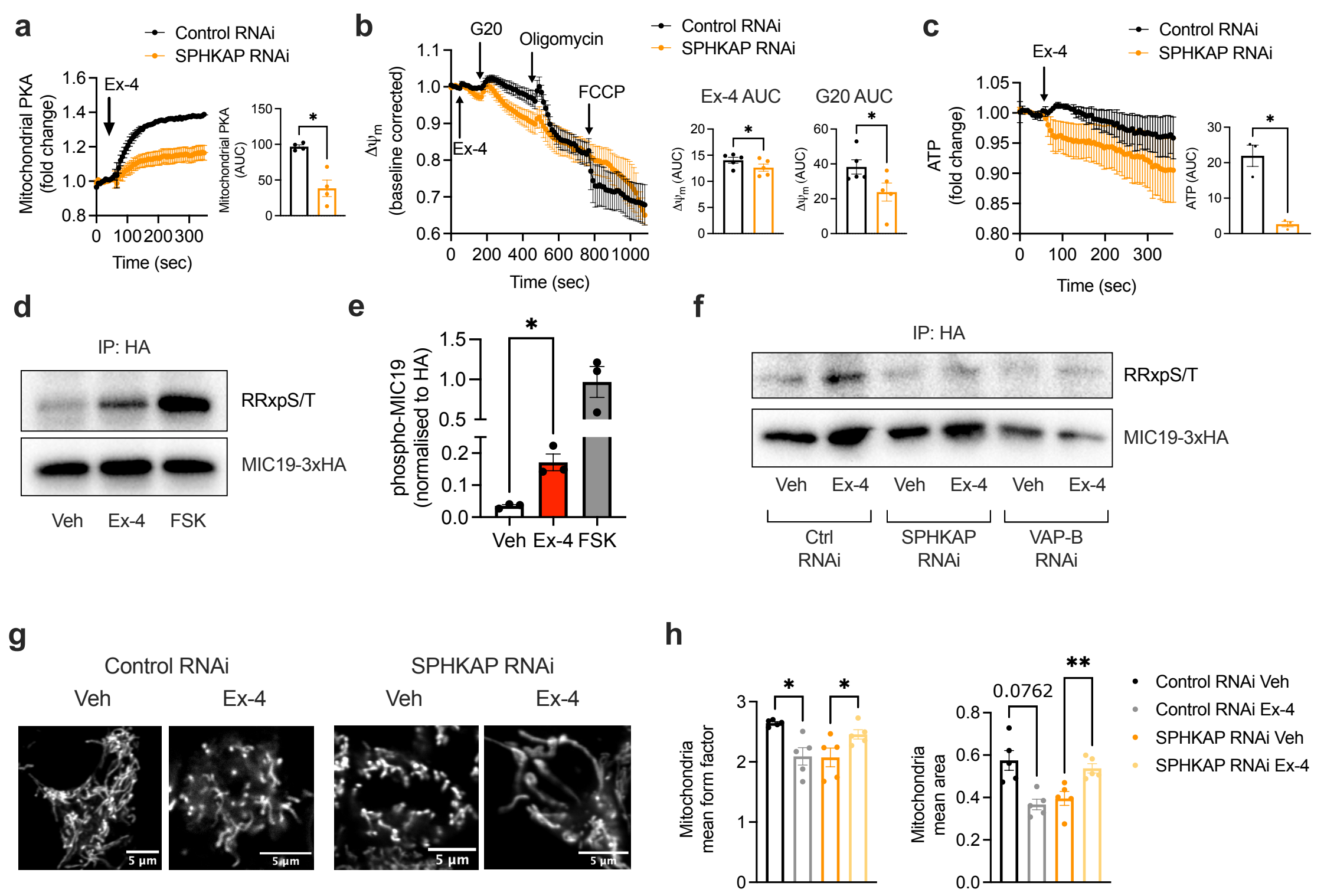
a
Control RNAi
SPHKAP RNAi
Ex-4
Mitochondrial PKA (fold change)
Time (sec)
Mitochondrial PKA (AUC)
b
G20
Oligomycin
FCCP
Ex-4
Δψm (baseline corrected)
Time (sec)
Ex-4 AUC
G20 AUC
Δψm (AUC)
c
Ex-4
ATP (fold change)
Time (sec)
ATP (AUC)
d
IP: HA
RRxpS/T
MIC19-3xHA
Veh
Ex-4
FSK
e
phospho-MIC19 (normalised to HA)
Veh
Ex-4
FSK
f
IP: HA
RRxpS/T
MIC19-3xHA
Veh
Ex-4
Veh
Ex-4
Veh
Ex-4
Ctrl RNAi
SPHKAP RNAi
VAP-B RNAi
g
Control RNAi
SPHKAP RNAi
Veh
Ex-4
Veh
Ex-4
5 µm
h
Mitochondria mean form factor
Mitochondria mean area
0.0762
Control RNAi Veh
Control RNAi Ex-4
SPHKAP RNAi Veh
SPHKAP RNAi Ex-4

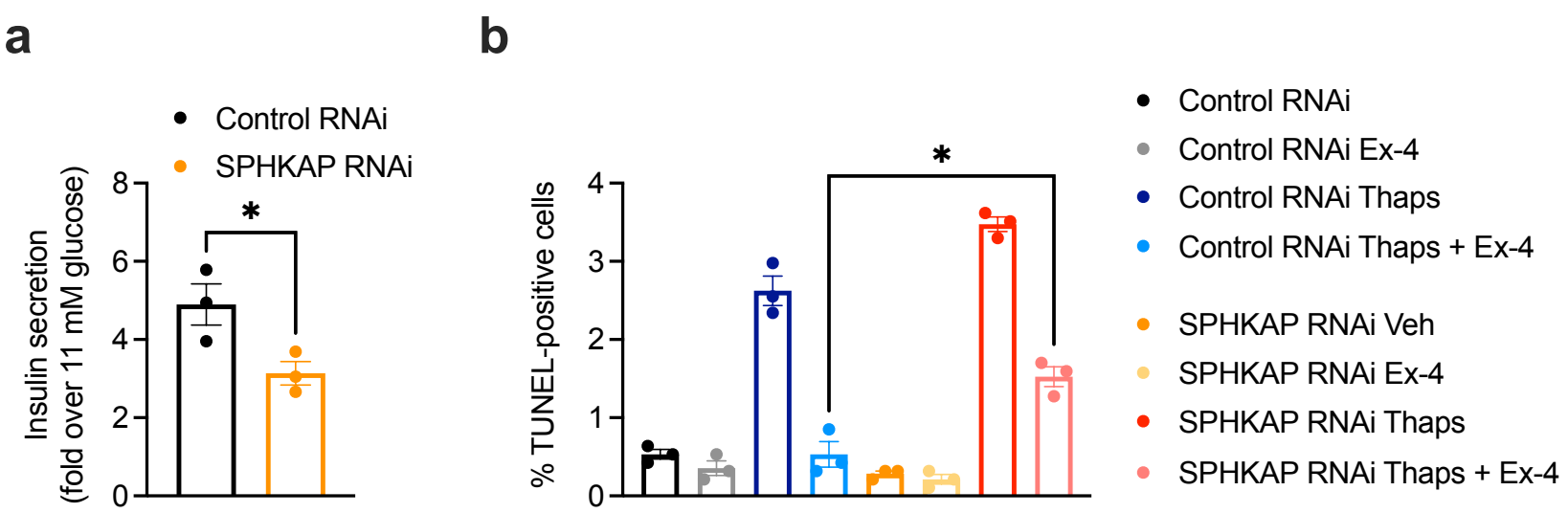
a
Control RNAi
SPHKAP RNAi
Insulin secretion
(fold over 11 mM glucose)
8
6
4
2
0
*
b
% TUNEL-positive cells
4
3
2
1
0
*
Control RNAi
Control RNAi Ex-4
Control RNAi Thaps
Control RNAi Thaps + Ex-4
SPHKAP RNAi Veh
SPHKAP RNAi Ex-4
SPHKAP RNAi Thaps
SPHKAP RNAi Thaps + Ex-4

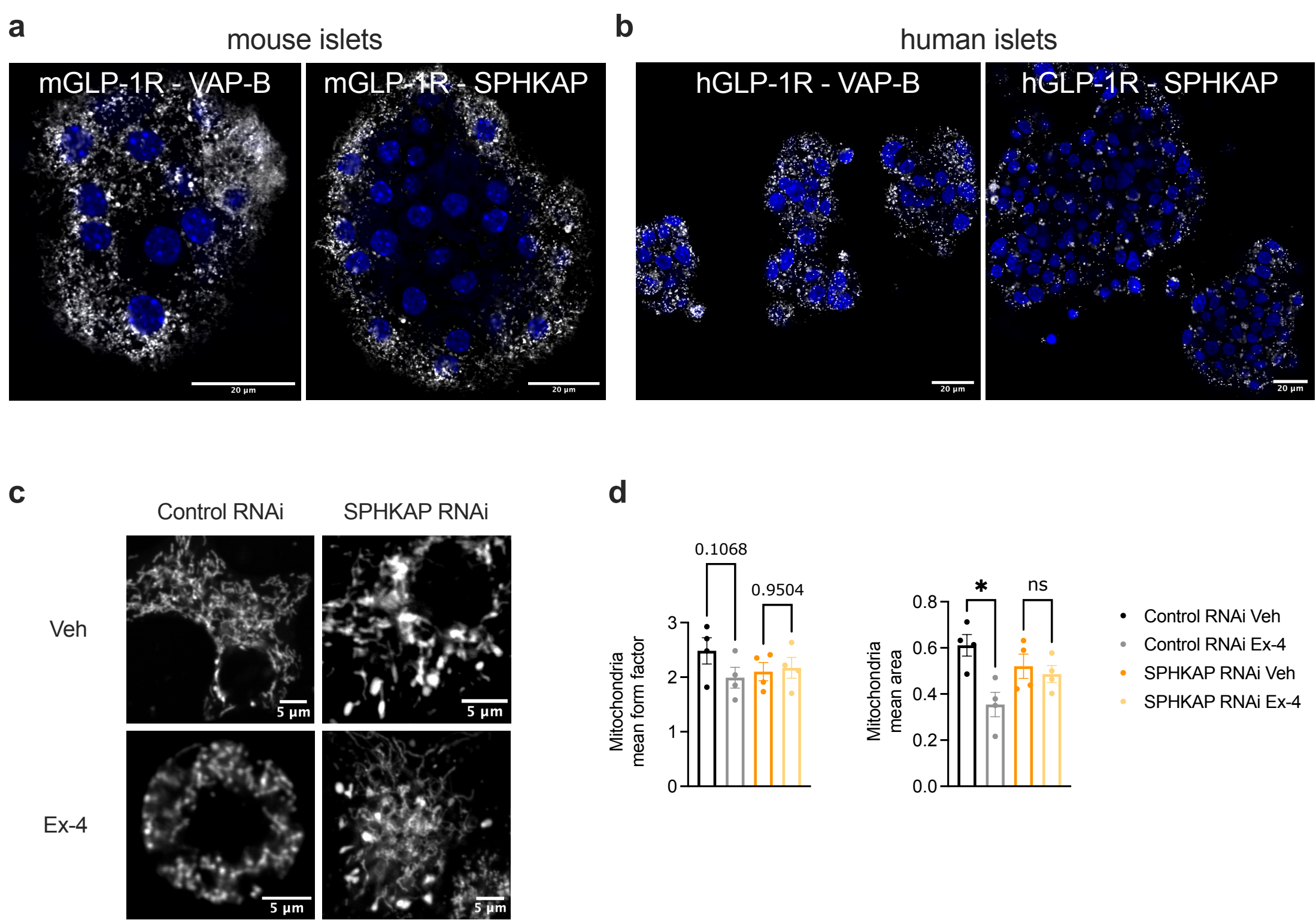
a
mouse islets
mGLP-1R - VAP-B
mGLP-1R - SPHKAP
20 µm
20 µm
b
human islets
hGLP-1R - VAP-B
hGLP-1R - SPHKAP
20 µm
20 µm
c
Control RNAi
SPHKAP RNAi
Veh
Ex-4
5 µm
5 µm
5 µm
5 µm
d
0.1068
0.9504
Mitochondria mean form factor
0
1
2
3
*
ns
Mitochondria mean area
0.0
0.2
0.4
0.6
0.8
Control RNAi Veh
Control RNAi Ex-4
SPHKAP RNAi Veh
SPHKAP RNAi Ex-4